Anisotropic nonlinear optical response of nodal-loop materials

Tommy Tai [1,*] and Ching Hua Lee [2,†]

[1]*Cavendish Laboratory, University of Cambridge, JJ Thomson Avenue, Cambridge CB3 0HE, United Kingdom*

[2]*Department of Physics, National University of Singapore, Singapore 117542, Singapore*

(Received 10 July 2020; accepted 15 April 2021; published 12 May 2021)

Nodal line semimetals have lately aroused much experimental and theoretical interest, with their gap closing along unconventional trajectories in the three-dimensional Brillouin zone. These trajectories or nodal lines can close into loops and trace out intricate knotted or linked configurations with complicated topologies. In this paper, we investigate the semiclassical optical response of two nodal loops in linked, unlinked, and touching configurations, focusing particularly on the interplay of response anisotropy and nonlinearity. We provide a geometric picture that unifies these aspects and sheds light on the effects of nodal topology and geometry. Based on a model abstracted from generic multi-nodal-loop scenarios, both with or without linkages, our findings will be applicable for a large class of nodal semimetal materials with multiple nodal lines or loops.

DOI: 10.1103/PhysRevB.103.195125

I. INTRODUCTION

Topological materials are among the most intensely researched current topics and encompass not just topological insulators [1–10] but also semimetals with topological nontrivial nodal structures [11–15]. Such nodal materials have provoked widespread studies due to their unconventional density of states and band structure, which have led to new or enhanced avenues for nonlinear optical responses, electron tunneling behavior, high-order-harmonic generation, superconductivity, and quantum Hall effects [13,16–28]. The potentially intricate topology of nodal loops in three-dimensional (3D) space has also inspired their design and realization in metamaterials and lossy or nonreciprocal media [29–46].

Despite their seemingly exotic nature, various nodal-line semimetal (NLSM) materials have recently been experimentally characterized, such as $PbTaSe_2$ [47,48], BiTeI [49], Mg_3Bi_2 [50–52], ZrSiTe and ZrSiSe [53,54], ZrSiS [55–57], BaAgAs [58], TaN [59], Ca_3P_2 [60,61], $SrAs_3$ [62,63], CaAgX (X = P, As) [64,65], the ZrGeX_c (X_c = S, Se, Te) family [66,67], magnetic semimetals EuB_6 [68], spin gapless semimetals [69], the centrosymmetric superconductor $SnTaS_2$ [70], and $PbTaS_2$ [71]. In the form of closed loops, they have also been observed as nodal links in CaAuAs [72], nodal chains in TiB_2 [73,74], and nodal line networks in RuO_2 [75]. Other materials such as the Ti_3X (X = Al, Ga, Sn, Pb) family [76], YH_3 [77], $YoCoC_2$ [78], MnN [79], $TiTaSe_2$ [80], the CaP_3 family [81], *ABC*-stacked graphdiyne [82], and layered X_2Y (X = Ca, Sr, Ba; Y = As, Sb, Bi) [83] have also been theoretically proposed to possess nodal loops.

In some of these NLSMs, the conduction and the valence bands intersect to form potentially very intricate structures, even more intricate than common examples in knot theory and prototypical nodal knot setups [43,84–87]. For instance, the material Co_2MnGa was theorized [88] to possess a complicated network of 3D band crossings characterized by various types of nontrivial nodal linkages and coupled chains enabled by perpendicular mirror planes. This was subsequently confirmed experimentally [89]. Another proposal of interlocking nodal chains may be realized in carbon networks, consisting of armchair graphene nanoribbon [90]. While transport and optical response properties are already well studied for simpler NLSMs [15,57,67,68,91–94], those of more complicated nodal-*loop* semimetals are still not well understood. Recently, it was proposed that topological nodal linkages can significantly enhance optical response nonlinearity and hence high-order-harmonic generation (HHG) [95]. However, the nonlinear response does not afford any topological quantization, unlike the linear response via the Kubo formula, and a complete understanding of the response properties of realistic nodal-loop material necessitates a systematic study of how the geometry of the nodal structure and its topology interplay and lead to various anisotropic and nonlinear behaviors.

As such, this work shall be concerned with a systematic investigation of how the relative shapes and linkage of nodal loops can lead to various anisotropic and nonlinear response components and how the various responses come together into a bigger picture that reveals the overall nodal topology and geometry. Following a review of semiclassical response theory in Sec. II, we introduce a canonical model of two nodal loops whose linkage and shapes can be independently tuned. This model serves as an abstraction of the multiple nodal touchings and linkages in realistic nodal materials, for instance, Co_2MnGa. In Sec. III, we study the various components in the response tensor of our model system, some of whose nonlinear properties have never been investigated. In Sec. IV, we show how these results help piece together a response surface whose evolution with field strength encapsulates the full information about the response anisotropy and nonlinearity,

*ytt26@cam.ac.uk
†phylch@nus.edu.sg

and to some extent the nodal structure and its dispersion. For our model, the direction which the response surface points towards in the high-field limit depends on whether the nodal structure is topologically linked.

II. NONLINEAR SEMICLASSICAL OPTICAL RESPONSE

To systematically relate the Hopf link response to its detailed momentum-space profile, we first review the theory of nonlinear semiclassical response and next introduce our model with tunable nodal linkage. Similar semiclassical approaches have been highly successful in explaining phenomena such as Hall effects and quantum oscillations in diverse settings [96–100], as well as Bloch oscillations and Berry curvature effects in the context of HHG [101,102]. HHG refers to the high-order-harmonic generation induced by strong nonlinear interactions when a very intense laser pulse is focused into a sample.

A. Semiclassical response theory

The nonlinear response of nodal materials emerges even at the semiclassical level, where many-body processes are simply encapsulated by a nonequilibrium occupation function $F\{\varepsilon[\mathbf{k}-e\mathbf{A}(\mathbf{t})]\}$ that weighs different contributions to the response optical current [103]:

$$\mathbf{J}=\int F\{\varepsilon[\mathbf{k}-e\mathbf{A}(\mathbf{t})]\}\langle\mathbf{k}|\hat{\mathbf{J}}|\mathbf{k}\rangle d^3\mathbf{k}. \tag{1}$$

Here, $F(\varepsilon)=(1+e^{\beta[\varepsilon(\mathbf{k})-\mu]})^{-1}$ is the *equilibrium* Fermi-Dirac occupation function that depends on the energy dispersion $\varepsilon(\mathbf{k})$, and $e\mathbf{A}(t)=e\int_{-\infty}^{t}\mathbf{E}(t')dt'$ is the impulse on an electron e due to an external electric field $\mathbf{E}(t)$. In frequency space, we can always replace $\mathbf{A}$ with $\mathbf{E}/i\Omega$. The current operator for a given Hamiltonian $\hat{H}$ is $\hat{\mathbf{J}}=\frac{\partial\hat{H}}{\partial\mathbf{k}}$, which reduces to the dispersion velocity $\langle\mathbf{k}|\hat{\mathbf{J}}|\mathbf{k}\rangle=\mathbf{v}(\mathbf{k})=\frac{\partial\varepsilon(\mathbf{k})}{\partial\mathbf{k}}$ in the translation-invariant intraband case. We express this optical response in material-dependent units of $nev_F\sim 10^{12}$ A m^{-2}, where n and v_F are the charge carrier density and the Fermi velocity, respectively. In real materials, we have v_F being 2.22×10^5 and 4.0×10^5 ms^{-1} in ZrGeSe [104] and CaAgAs [93], respectively, and n being 3.37×10^{26}, 2.98×10^{26}, and 1.7×10^{26} m^{-3} in YbCdGe [92], CaCdSn [94], and CaAgAs [93], respectively. In these NLSMs, the Fermi surface is a simple nodal loop. The optical response of real materials with more sophisticated nodal structure, beyond the simplest nodal loop, have also been computed in Ref. [95]. Compared with the response predicted for graphene, using Eq. (1), the optical response for a graphene monolayer [105] is only $\sim10^9$ A m^{-2}, a few orders of magnitude smaller.

Equation (1) holds in the ballistic limit, where it is the exact solution to the semiclassical Boltzmann equation and the semiclassical equations of motion for electronic wave packets [103]. This requires $\Omega\tau\gg1$, where Ω is the optical frequency defined by $\mathbf{E}(t)\sim\mathbf{E}(0)e^{i\Omega t}$ and τ is the relaxation time due to impurity scattering. For a nodal material with relaxation time $\tau\sim10^{-12}$–10^{-13} s, comparable to that in high-quality graphene samples [106], $\Omega\tau\gg1$ can be achieved in the terahertz regime of $\Omega\sim$ 50–100 THz. The relaxation times can be computed from a microscopic model for the scattering processes [107]. In this ballistic regime, scattering processes cannot catch up with the much shorter oscillation timescales [102,108].

According to Eq. (1), the response current arises from contributions at $\mathbf{k}$ for which the Fermi-Dirac occupation $F[\varepsilon(\mathbf{k})]$ is nonvanishing. As such, it strongly depends on the shape of the (occupied) Fermi region in the Brillouin zone (BZ), particularly its codimensionality. This intraband response is the expectation of $\mathbf{v}[\mathbf{k}+\mathbf{e}\mathbf{A}(t)]$ within the occupied region that is dynamically shifted by the external electromagnetic impulse. When the occupied region is not a "blob" in the BZ but a thin Fermi "tube" of nontrivial codimension, the expectation of $\mathbf{v}[\mathbf{k}+\mathbf{e}\mathbf{A}(t)]$ can fluctuate wildly with $\mathbf{A}(t)$ due to "destructive interference" of $\mathbf{v}$ at different $\mathbf{A}(t)$ shifts, as previously pointed out in Refs. [95,103,109]. In Ref. [103], this observation was first used to explain the nonlinear response of graphene due to its vanishing density of states at small chemical potential. This was generalized in Ref. [109] to nodal-loop structures, i.e., where two bands intersect along a loop in the BZ, where a stronger nonlinearity from a characteristic nonlinear response curve was reported. In Ref. [95], this nonlinear response was further shown to be strongly enhanced in a 3D material with nontrivial nodal topology, i.e., when band intersections form loops that are topologically linked.

To more concretely understand why nodal structures with nontrivial linkages have strong nonlinear responses, consider small chemical potentials μ such that the occupied states take the form of nodal "tubes" along nodal lines, which are then shifted by the electromagnetic impulse $\int^t\mathbf{E}(t')dt'$ away from the original nodal structure in the BZ. By differentiating Eq. (1) with respect to the vector potential, we obtain [95], for small μ,

$$\frac{\partial J_i}{\partial A_j}\approx 2\sum_{\alpha\in\mathrm{NLs}}\frac{\mu}{\hat{e}_j\cdot\mathbf{v}_\mathbf{F}}\frac{\partial^2\varepsilon(\mathbf{k}^\alpha+e\mathbf{A})}{\partial k_i\partial k_j}, \tag{2}$$

where $\mathbf{k}^\alpha$ labels the trajectories of all the nodal lines α in the BZ and $\hat{e}_j\cdot\mathbf{v}_F$ is the component of the Fermi velocity of the αth nodal line (NL) at momentum $\mathbf{k}^\alpha$ along the applied field. In Eq. (2), the differential (optical) response tensor of a nodal line structure is given by a sum over the Hessian of the dispersion at the nodal lines shifted by $\mathbf{A}$ in the BZ. Evidently, we expect the response to be nonlinear whenever $\frac{\partial J_i}{\partial A_j}$ is significantly nonconstant, which has to be the case around nodal crossings with vanishing gap. In particular, in the diagonal sector where $i=j$, $\varepsilon(\mathbf{k}^\alpha+e\mathbf{A})$ has to pass through a singularity whenever two nodal loops are linked in the direction $\mathbf{A}$, since the locus of $\mathbf{k}^\alpha+e\mathbf{A}$ for one of the loops α must intersect another loop α' as $\mathbf{A}$ increases. This leads to the enhancement of diagonal response nonlinearity in topologically linked nodal loops, which can be quantified by the extent of HHG it causes.

However, the abovementioned argument for nonlinearity enhancement pertains only to the diagonal $i=j$ sector, where the response is probed in the direction where the applied field displaces the nodal loops. It remains an open question whether a nodal linkage also possesses signature response behaviors in the other directions, in both longitudinal and transverse sectors. In this paper, we shall focus on elucidating the signature contributions to the optical response due to a

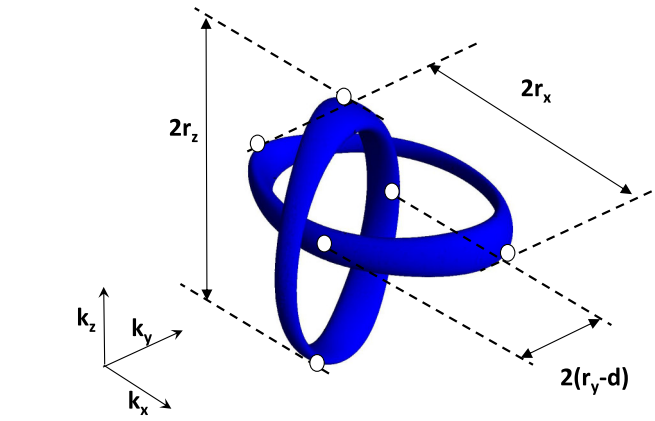

(a)

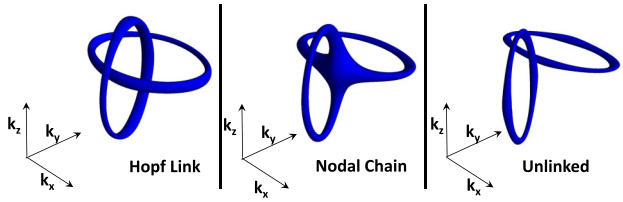

(b)

FIG. 1. (a) The Fermi surface of the Hopf link in **k** space, with the parameters r_x, r_y, r_z, and d as labeled. We assumed $r_x = r_z$. The quantity $2(r_y - d)$ controls the extent of linkage in the Hopf link. (b) The three distinct possibilities of the Hopf structure are as follows: Hopf link ($r_y < d$), nodal chain ($r_y \approx d$), and unlinked nodal loops ($r_y > d$), illustrated here for a nonvanishing $\mu = 0.1$.

generic nodal linkage, particularly on how nontopological contributions from the dispersion profile compete with those from the topological linkage. While real nodal materials may also experience response contributions from the Berry curvature and interband scattering, these additional contributions are very material dependent and do not form the focus of this work, which aims to explore the most generic response behavior expected from nodal linkages.

B. Canonical Hopf link model

In this paper, we have chosen to focus on the simplest topologically nontrivial nodal linkage, which is the Hopf link—a nodal configuration consisting of two nodal loops that will be linked when they are sufficiently close to each other. By introducing a canonical two-band Hopf link model where the key parameters r_y, r_x, and d [Fig. 1(a)] are all independently adjustable, we can isolate the various geometric and topological factors that influence its nonlinear response. The parameters are as follows:

(i) r_y is the width of the loops in the k_y direction or longitudinal direction along which the two loops are separated;

(ii) r_x is the width of the loops in the k_x or k_z transverse directions;

(iii) $2d$ is the displacement between the two loops, centered at $(0, \pm d, 0)$. They are linked if $r_y > d$, since the longitudinal separation between them is given by $2(r_y - d)$ (Fig. 1).

Our two-band nodal Hopf link Hamiltonian takes the form

$$H_{\text{Hopf}}(\mathbf{k}) = h(k_x, k_y, k_z)\sigma_x + g(k_x, k_y, k_z)\sigma_y, \tag{3}$$

where the functions $h(\mathbf{k})$ and $g(\mathbf{k})$ are obtained by deforming a well-known Hopf link model derived through the Hopf map [43,110–112], for which the Hopf link parameters cannot be easily adjusted independently [113]. The gap $2\epsilon(\mathbf{k}) = 2\sqrt{g(\mathbf{k})^2 + h(\mathbf{k})^2}$ closes along two loops given by the simultaneous solutions of $g(\mathbf{k}) = 0$ and $h(\mathbf{k}) = 0$. Explicitly, with the intermediate parameters $\xi = \frac{\cos r_y - 1}{\cos r_x - 1}\frac{1}{\sin d} - 1$ and $\Gamma = \frac{\cos r_x \cos r_y - 1}{\cos r_x - 1}\frac{1}{\sin d}$, $h(\mathbf{k})$ and $g(\mathbf{k})$ are given by

$$h(k_x, k_y, k_z) = \sin^2(k_z - k_x) - (\xi\cos(k_x + k_z) + \cot d\cos(k_y) + \cos(k_z - k_x) - \Gamma)^2 - \sin^2(k_x + k_z) + \sin^2(k_y), \tag{4a}$$

$$g(k_x, k_y, k_z) = 2\sin(k_z - k_x)(\xi\cos(k_x + k_z) + \cot d\cos(k_y) + \cos(k_z - k_x) - \Gamma) - 2\sin(k_x + k_z)\sin(k_y). \tag{4b}$$

At chemical potential $\mu = 0$, the two nodal loops lie in the planes $k_x = 0$ and $k_z = 0$, with a common mirror symmetry axis along the k_y line. The nodal loops each touch this symmetry axis at two points, giving rise to a total of four touching points $\pm(r_y \mp d)$. From Fig. 1, $r_y - d$ evidently describes the extent of their linkage. When $r_y > d$, the two nodal loops are linked together, and we call this resulting arrangement a Hopf link.

In realistic materials, the chemical potential μ can often be tuned away from the nodal energy, so as to obtain a finite density of states available for transport. For generic linearly dispersive nodal systems, μ scales with the thickness of the nodal tube. A large μ tends to result in thick tubes that inevitably intersect, resulting in a nodal chain even when $r_y \neq d$.

In total, there are three possibilities as illustrated in Fig. 1(b):

(*i*) *Hopf link*. The two nodal loops are topologically linked ($r_y > d$ for $\mu \ll 1$).

(*ii*) *Unlinked nodal loops*. The two nodal loops are disjoint and not topologically linked ($r_y < d$ for $\mu \ll 1$).

(*iii*) *Nodal chain*. The two nodal loops touch each other at a point and are not topologically linked ($r_y \approx d$ for $\mu \ll 1$).

Due to the periodicity of its various terms, the Hamiltonian can sometimes admit additional solutions, i.e., "*periodic images*" within the first BZ. These solutions, analogous to the degenerate valleys in graphene, occur as two distinct types, as further elaborated in Appendix A. To prevent the confounding ambiguities resulting from the interference of multiple nodal linkages, we shall exclusively study only cases where such periodic images do not exist.

For the rest of this paper, we shall set the temperature to a representative value of 10 K, i.e., $\beta := \frac{\text{eV}}{k_B T} = 1160$, which can be adjusted to fit the physical temperature of an actual physical scenario by trivially rescaling our canonical model. For definiteness, we choose a chemical potential of $\mu = 0.1$ eV, such that the nodal structure consists of thin closed tubes

that exhibit distinct crossovers in topology (linked, intersecting, unlinked) as they are shifted due to photon excitations. However, our results shall continue to hold even when typical photon energies are much smaller than μ. We shall study the behavior of the optical response as the three independent parameters $\{d, r_x, r_y\}$ are varied, insofar as the parameters do not admit periodic images, for all three types of cases (linked, unlinked, and nodal chain).

III. OPTICAL RESPONSE IN VARIOUS DIRECTIONS

We next investigate the various diagonal and off-diagonal (Hall) responses of the nodal Hopf link in the principal directions—both longitudinal (along the direction of loop separation $\hat{y}$) and transverse directions (perpendicular to the direction of loop separation $\hat{x}$ and $\hat{z}$).

Consider a sinusoidal time-varying applied electric field signal $\mathbf{E}(t) = \mathbf{E_0} \cos \Omega t$, which corresponds to the vector potential $\mathbf{A}(t) = \mathbf{A} \sin \Omega t$, where $\mathbf{A} = \mathbf{E_0}/i\Omega$. In the presence of an oscillatory electric field $\mathbf{E}(t)$, the minimally coupled Fermi-Dirac occupation in Eq. (1) will be $F\{\varepsilon[\mathbf{k} - e\mathbf{A}(t)]\}$, which is equivalent to a translation of the Fermi tube of occupied states in the field direction according to the momentum shift $\mathbf{k} \to \mathbf{k} - e\mathbf{A}(t)$. This picture motivates the $\mathbf{A}$ dependence of $\mathbf{J}$ rather than $\mathbf{E}$. The ballistic criterion $\Omega \sim 100$ THz is independent of the nodal energy since the Fermi surface is translationally invariant. Although there are nine possible response components $J_i(A\hat{j})$, $i, j \in x, y, z$, some of them necessarily generically vanish or are not independent due to the symmetries of our Hamiltonian [Eq. (3)]:

$$J_x(A\hat{y}) = 0, \quad J_z(A\hat{y}) = 0, \tag{5a}$$

$$J_x(A\hat{x}) = J_z(A\hat{z}), \tag{5b}$$

$$J_z(A\hat{x}) = J_x(A\hat{z}), \tag{5c}$$

$$J_y(A\hat{x}) = -J_y(A\hat{z}). \tag{5d}$$

Equation (5a) holds since the nodal loops have mirror symmetry about the $k_x = 0$ and $k_z = 0$ planes, respectively. As the dispersion velocity $\langle \mathbf{k}|\hat{\mathbf{J}}|\mathbf{k}\rangle$ [Eq. (1)] inherits the same symmetry as the Fermi surface—mirror symmetry about the k_y axis—when the Fermi surface is displaced along the longitudinal k_y axis (Fig. 2), the resulting contribution by the Fermi tubes on the left of the k_y axis will exactly cancel that due to the Fermi tubes on the right. Equations (5b) and (5c) follow from the symmetrical roles played by transverse momenta k_z and k_z. Equation (5d) is true because the loops are related to each other by interchanging $k_x \leftrightarrow -k_z$. In all, there are only four unique current responses in the following response matrix:

$$J_i(A\hat{j}) = \begin{pmatrix} J_x(A\hat{x}) & J_y(A\hat{x}) & J_z(A\hat{x}) \\ 0 & J_y(A\hat{y}) & 0 \\ J_z(A\hat{x}) & -J_y(A\hat{x}) & J_x(A\hat{x}) \end{pmatrix}. \tag{6}$$

Since A scales with E_0 for our sinusoidal electric field, Eq. (6) is similar to a conductivity tensor. As we shall show, the diagonal responses are much more affected by the topological linkage of the nodal loops, compared with the nondiagonal response, i.e., Hall responses.

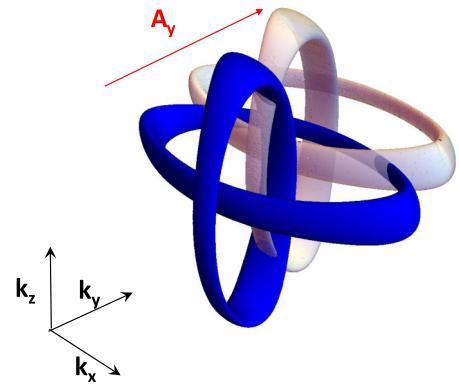

FIG. 2. Contribution to the semiclassical response [Eq. (1)]: In the presence of an illustrative applied field along the k_y direction, the Fermi surface is displaced along the k_y axis in $\mathbf{k}$ space in a manner symmetric about the $k_x = 0$ and $k_z = 0$ planes. This accounts for the vanishing responses J_x and J_z.

A. Transverse diagonal responses $J_x(A\hat{x})$, $J_z(A\hat{z})$

According to Eq. (1), we generically expect a nonlinear semiclassical response since its integral is a highly nonlinear function. This is especially the case for a Hopf link, where each nodal loop juts out of the plane of the other nodal loop. As such, it acts as a source of dispersion velocity $\langle \mathbf{k}|\hat{\mathbf{J}}|\mathbf{k}\rangle$, which "destructively interferes" with those due to the nodal loop that encloses this nodal tube [95]. When the Fermi surface of the Hopf link starts to translate by the impulse from an applied field [Fig. 3(a)], the response, computed from Eq. (1), initially increases sharply followed by a much slower nonmonotonic change until the applied field is sufficiently large that the Fermi surface begins to leave the region of influence exerted by the singularity.

Beyond that, the contribution of $\langle \mathbf{k}|\hat{\mathbf{J}}|\mathbf{k}\rangle$ continues to add up, giving a subsequent monotonic response. The extent of nonlinearity afforded by each singularity is described by Eq. (2), where the gradient is a sum of the second derivatives of the dispersion. The transverse (perpendicular to the direction of the loop separation) diagonal optical response of the Hopf link was found to observe the following general trends [we plot the most nonlinear responses in Figs. 3(b)–3(d)]:

(1) The response demonstrates a weak dependence on the longitudinal separation d when the nodal loops are topologically linked, but not true otherwise, as illustrated in Figs. 3(b) and 3(f), respectively.

(2) The extent of response nonlinearity is enhanced with larger transverse radius r_x or smaller longitudinal radius r_y, i.e., larger loop aspect ratio r_x/r_y, as illustrated in Figs. 3(c) and 3(d). Correspondingly, the response currents generally decrease with increasing nonlinearity.

We can physically understand these trends. Since the relative separation d of the centers of the loops merely changes the relative longitudinal k_y position of the loops, intuitively it should not play a significant role in influencing the transverse response resulting from the transverse translation of the Fermi surface. Indeed, the transverse diagonal response is almost independent of d [Fig. 3(b)] in the Hopf link. Yet, this independence from d no longer holds when the loops are no

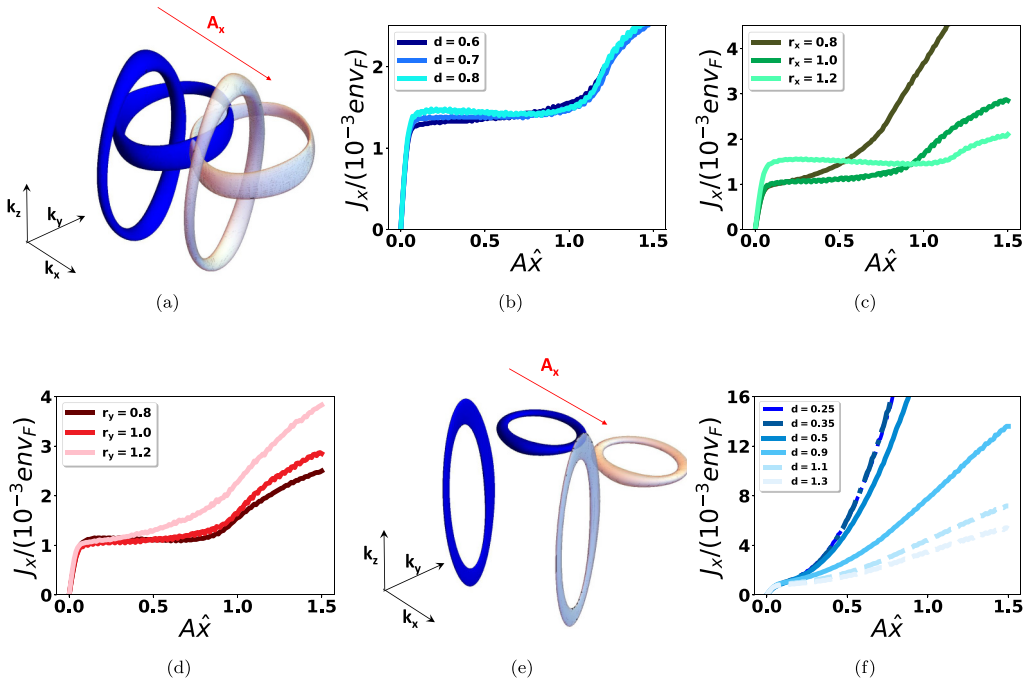

FIG. 3. (a) In the presence of an applied transverse field $A\hat{x}$, the Fermi surface of the Hopf link is displaced along the transverse k_x axis in $\mathbf{k}$ space, in turn giving rise to a transverse diagonal optical response $J_x(A\hat{x})$. (b) For the Hopf link, the transverse response weakly depends on d, for $r_x = 0.8$ and $r_y = 1.2 > d$. (c) Enhancement of transverse response nonlinearity for the Hopf link as r_x increases, for $d = 0.5 < r_y = 1.0$. (d) Enhancement of transverse response nonlinearity for the Hopf link with $r_y > d = 0.5$ and $r_x = 1.0$. (e) Displacement of the Fermi regions of the unlinked nodal loops along the transverse k_x axis in $\mathbf{k}$ space, with the singularities from each loop becoming weaker as the loops are farther separated. (f) The transverse response shows a stronger dependence on d when the nodal loops are no longer topologically linked. As the longitudinal loop separation increases, the response currents become smaller. Here, we contrast the responses of the Hopf link (dash-dotted lines, $d = 0.25, 0.35$), unlinked nodal loops (dashed lines, $d = 1.1, 1.3$), and the nodal chain (solid lines, $d = 0.5, 0.9$) for $r_y = 0.6$, $r_x = 0.4$. For (b)–(d), the chosen parameter sets are among those that exhibit the greatest nonlinearity in the transverse response. The responses are in units of env_F, where n and v_F are the number density and Fermi velocity of the NLSM material, respectively.

longer topologically linked [Figs. 3(e) and 3(f)] because farther separated loops, i.e., sources of singularities, correspond to more uniform velocity fields, in turn leading to smaller response currents. This is unlike the linked cases, where the nodal linkage guarantees the proximity to nodal singularities and topologically "protects" the transverse response (previous literature, i.e., Ref. [95], only reported the topological enhancement of the longitudinal response).

On the other hand, increasing the transverse radius r_x or decreasing the longitudinal radius r_y stretches the aspect ratio of each loop and hence the boundary for "interference" (defined by the locus of points where the competition of opposing dispersion velocity vectors terminates) along the transverse k_x direction, giving more room for destructive interference as the Fermi surface is displaced along the transverse k_x direction. This in turn gives a greater range of $A\hat{x}$ where the response undergoes a nonmonotonic change.

B. Longitudinal diagonal response $J_y(A\hat{y})$

Unlike in the transverse diagonal response, the longitudinal separations of the loops $2(r_y - d)$ now greatly influence the longitudinal (along the direction of the loop separation) responses of the Hopf link. As before, these nodal tubes are sources of destructive interference for the dispersion velocity $\langle \mathbf{k}|\hat{\mathbf{J}}|\mathbf{k}\rangle$. The semiclassical response is again computed from Eq. (1) as the Fermi surface of the Hopf link is displaced along the longitudinal k_y direction [Fig. 4(a)]. The general trends for the longitudinal diagonal optical response of the Hopf link are as follows:

(1) The extent of response nonlinearity is enhanced with larger longitudinal loop separation d, as illustrated in Fig. 4(b).

(2) Increasing the longitudinal radius r_y also enhances the extent of response nonlinearity, as illustrated in Fig. 4(d).

(3) The transverse radius r_x does not change the shape of the response curves, but the magnitude of the response does increase with r_x, as illustrated in Fig. 4(c).

To physically explain these trends, note that as d increases with r_y fixed, the loop separation $2(r_y - d)$ decreases, enhancing the extent of nonlinearity due to the closer proximity of one loop with the band singularity of the other. While the nonlinearity is still present, as shown in Fig. 4(f), when the nodal loops are no longer topologically linked, this is an artifact from the weaker dispersion field when the loops are separated farther apart. Increasing r_y at fixed d also enhances the nonlinear response by providing a greater range of values of $A\,\hat{y}$ for significant destructive interference to occur.

On the other hand, r_x only stretches the nodal loop in the transverse k_x direction, which plays no role in the destructive interference in the longitudinal direction. Yet r_x increases the circumferential length of the nodal loop, which gives a greater

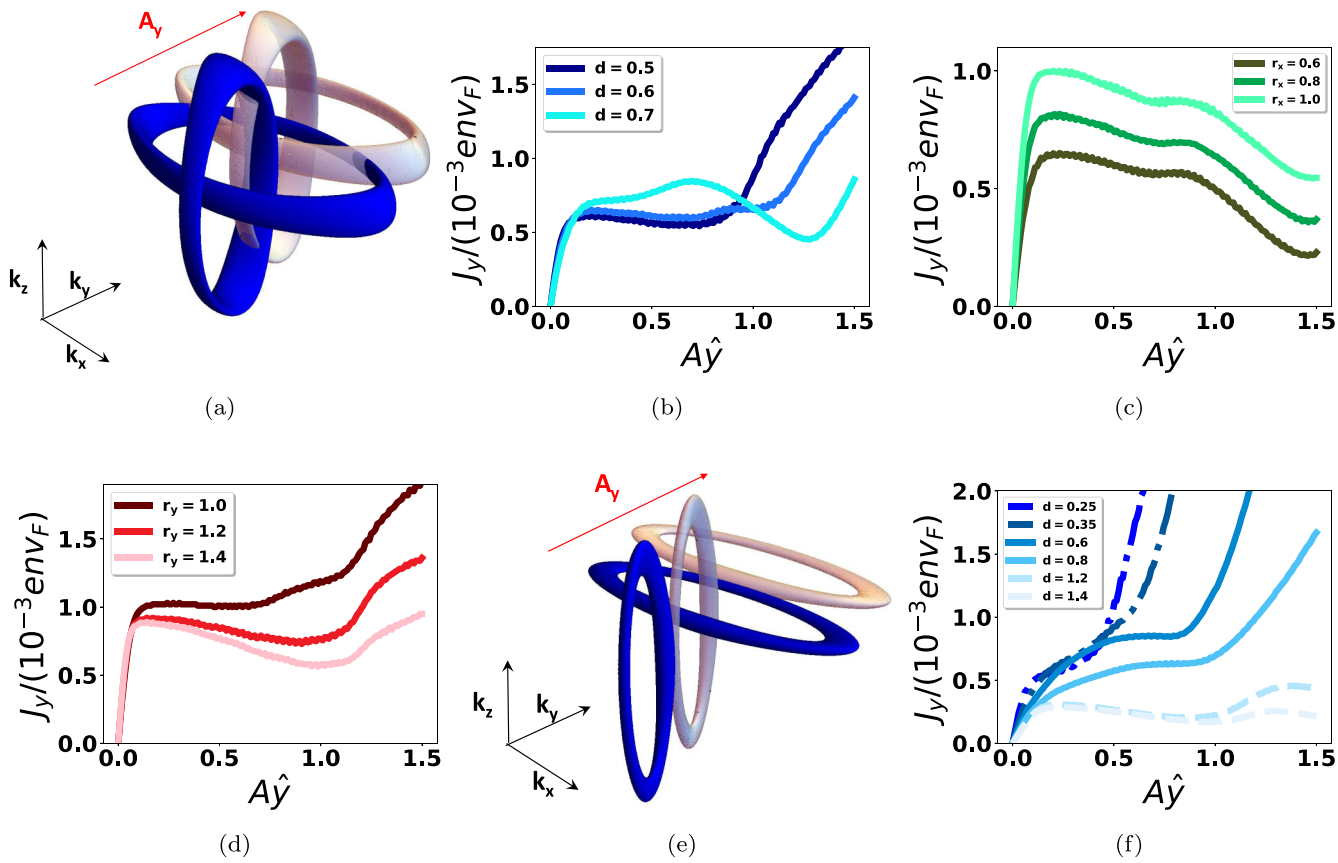

FIG. 4. (a) In the presence of an applied longitudinal field $A\hat{y}$, the Fermi surface of the Hopf link is displaced along the longitudinal k_y axis in $\mathbf{k}$ space, in turn giving rise to a longitudinal diagonal optical response $J_y(A\hat{y})$. (b) Enhancement of longitudinal response nonlinearity by increasing d in the linked regime with $r_y = 1.0 > d$, $r_x = 0.6$. (c) The shape of the longitudinal response for the Hopf link is independent of the transverse radius r_x but increases in magnitude with r_x, as plotted for $r_y = 1.2 > d = 0.8$. (d) Enhancement of longitudinal response nonlinearity for the Hopf link by increasing $r_y > d = 0.6$ at $r_x = 1.0$. (e) Displacement of the Fermi regions of the unlinked nodal loops along the longitudinal k_y axis in $\mathbf{k}$ space, with the singularities from each loop becoming weaker as the loops are farther separated. (f) Comparing the longitudinal responses for the Hopf link (dash-dotted lines, $d = 0.25, 0.35$), unlinked nodal loops (dashed lines, $d = 1.2, d = 1.4$), and the nodal chain (solid lines, $d = 0.4, d = 0.8$) for $r_y = 0.6$, $r_x = 0.4$. The longitudinal response decreases in magnitude but becomes more nonlinear as d increases. This increasing nonlinearity is an artifact of the weaker influence of the singularities as the loops are farther separated. For (b)–(d), the chosen parameter sets are among those that exhibit the greatest nonlinearity in the transverse response. The responses are in units of env_F, where n and v_F are the number density and Fermi velocity of the NLSM material, respectively.

contribution to $\mathbf{J}$ in Eq. (1) and hence a greater response magnitude.

IV. GLOBAL ASPECTS OF OPTICAL RESPONSE ANISOTROPY

Having discussed the nonlinearity of the response tensor along the principal directions, we now present how the anisotropic response behaves as a whole. Due to nonlinearity, i.e., $\mathbf{J}(\mathbf{A}_1 + \mathbf{A}_2) \neq \mathbf{J}(\mathbf{A}_1) + \mathbf{J}(\mathbf{A}_2)$, the responses in directions away from the previously studied principal directions $\hat{\mathbf{A}} = (1, 0, 0)$, (0,1,0), and (0,0,1) may behave unexpectedly. In the following, we shall represent the response across all directions in the form of constant $|\mathbf{A}| = A_0$ level surfaces in $\mathbf{J}$ space [recall that $\mathbf{A}(t) = \int_{-\infty}^{t} \mathbf{E}(t')dt'$]. We parametrize this surface $\mathcal{S}_A$ with spherical angular coordinates as follows:

$$\mathcal{S}_A = \{A_0\hat{\mathbf{A}} = A_0(\cos\theta\cos\phi, \cos\theta\sin\phi, \sin\theta)\}, \quad (7)$$

where $0 \leqslant \theta \leqslant \pi$, $0 \leqslant \phi \leqslant 2\pi$. The anisotropy in the optical response of our canonical double-nodal-loop model [Eqs. (3), (4a), and (4b)] due to $\boldsymbol{\alpha} = A_0\hat{\mathbf{A}}$ is described by the anisotropy of the smooth $\mathcal{S}_J$ surface embedded in the J space. We represent the azimuthal angle ϕ with a color map defined by $\mathcal{S}_A$ in Fig. 5(a), which will be significantly distorted by anisotropy when bijectively mapped onto $\mathcal{S}_J$ (Figs. 6 and 7).

Insight into the shapes of the constant A_0 response surfaces, as well as their significance with regard to nodal topology and geometry, can be obtained by computing the response in a few high-symmetry directions of $\hat{\mathbf{A}}$, such as $\hat{\mathbf{A}} = \pm(0, 1, 0), \pm(1, 0, 1), \pm(1, 0, -1)$ (for notational simplicity, we shall henceforth drop the normalization factor). From Eq. (5a), we know that for a longitudinal external field $\hat{\mathbf{A}} = \pm(0, 1, 0)$, there is a vanishing transverse response, i.e., $J_x = J_z = 0$ for such $\hat{\mathbf{A}}$. Hence the corresponding point on the $\mathcal{S}_J$ surface must be along the J_y axis, with $|J_y|$ being the width of the surface along the J_y axis. This is also the longitudinal diagonal current discussed in Sec. III. Also,

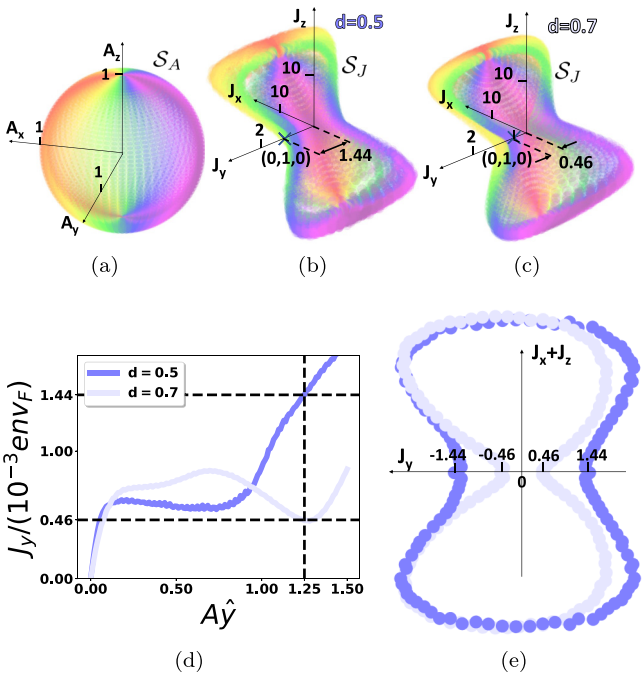

FIG. 5. (a) To draw the response surfaces, we represent an external field of constant magnitude A_0 but arbitrary direction as a sphere $\mathcal{S}_A$ in A space. The sphere is colored by the azimuthal angle ϕ and is significantly distorted by anisotropy when bijectively mapped onto the response surfaces $\mathcal{S}_J$ in 3D J space. (b) and (c) Illustrative examples of the distortion for our model [Eq. (3)] with $r_x = 0.6$, $r_y = 1.0$, $\mu = 0.1$, $A_0 = 1.25$, for $d = 0.5$ and 0.7, respectively (**J** in units of 10^{-3} env_F). (d) Origin of the thicker "waist" of (b) vs (c) in terms of $J_y(A_0\hat{y})$ response. At $A_0 = 1.25$, the $d = 0.5$ case (b) has a response current almost three times as large. (e) This difference in $J_y(A_0\hat{y})$ corresponds to a large difference in the thickness of the concave waist of the response surface, as more clearly illustrated by comparing cross sections of (b) and (c) at $\theta = \frac{\pi}{2}$.

the response surface point corresponding to $\hat{\boldsymbol{A}} = \pm(1, 0, 1)$ must lie in the J_x-J_z plane, since $J_y = 0$ from Eq. (5d). By Eq. (5b), there is an equal contribution of J_x and J_z from $\hat{\boldsymbol{A}} = \pm(1, 0, 1)$, so all corresponding points from this orientation of $\hat{\boldsymbol{A}}$ must lie on the 45° diagonals along the J_x-J_z axes, as evident in Figs. 6 and 7. Incidentally, points corresponding to $\hat{\boldsymbol{A}} = \pm(1, 0, -1)$ also lie in the J_x-J_z plane despite not being directly protected by Eqs. (5a) and (5d), a fine illustration of the nonlinearity of $\mathbf{J}(\mathbf{A})$. Other high-symmetry directions which we shall use in the following discussion include $\hat{\boldsymbol{A}} = \pm(1, 1, 0)$, $\pm(0, 1, 1)$, $\pm(1, -1, 0)$, $\pm(0, 1, -1)$.

Before starting the detailed analysis of the response surface, we consider a quick example. In Sec. III, we highlighted that a greater longitudinal separation d between two topologically linked nodal loops results in a more nonlinear response [Fig. 4(b)]. This is indeed seen in our corresponding $\mathcal{S}_J$ surfaces. At an illustrative $A_0 = 1.25$, this nonlinear response is approximately three times larger, i.e., less nonlinear for $d = 0.5$ vs $d = 0.7$ [Fig. 5(d)], which corresponds to a proportionally smaller width of the "waist" of the response surface in the $\hat{y}$ direction [Figs. 5(b) and 5(c)]. This is more evident when viewed in the cross-sectional plane $\hat{A} = (1, 0, 1)$ with only $\theta = \frac{\pi}{2}$ points plotted [Fig. 5(e)]. That the general shapes of the $d = 0.5$ and $d = 0.7$ surfaces appear rather similar [Figs. 5(b) and 5(c)] can be understood from the weak dependence on d for the transverse diagonal responses, as discussed in Sec. III. Clearly, the results from Sec. III alone are inadequate in working out the entire response surface, and thus the response surfaces provide a bigger picture and, as we will see, shed light on nodal topology and geometry.

A. Response surfaces and nodal topology

It is already known [95] that nodal linkages can enhance the nonlinearity of the response, at least in the longitudinal diagonal direction $J_y(A_0\hat{y})$ (Fig. 4). Furthermore, significant nonlinearity is also present in the transverse diagonal directions $J_x(A_0\hat{x})$ and $J_z(A_0\hat{z})$, although not necessarily enhanced by the topological linkage. Hence we shall expect such nonlinearity to be manifested in the constant A_0 response current surface too.

Indeed, as shown in Fig. 6, typical linked, touching, and unlinked nodal loops exhibit significantly different evolutions of the constant A_0 response surfaces as A_0 is increased. At small A_0, all three cases have ellipsoidal-shaped response surfaces, testimony to anisotropy of the nodal system, even in the linear (small A_0) limit. At very large A_0, i.e., $A_0 = 1.75$, where the Fermi regions have been displaced far from their original positions, the response surfaces are all very anisotropic and large, since minimal cancellation of the velocity field $d\varepsilon/d\mathbf{k}$ occurs. Their exact shapes depend on the details of the energy dispersion away from the loops and are nonuniversal though decidedly anisotropic. What is most interesting is the intermediate $A_0 \approx 0.75$ regime, which for the linked case is around when the Fermi region of one loop crosses the singularity from the other loop. For the linked case, the significant nonlinearity of the response around intermediate values of A (see Figs. 3 and 4) suppresses the response current, particularly in the longitudinal directions with "untwisted colors" in Fig. 7. As such, this leads to a somewhat "squeezed" appearance of the response surface compared with that of the nodal chain or unlinked cases, where the response surface looks comparatively "puffed up" during the A_0 evolution. Compared with the other cases, the unlinked case shows the least variation in response surface shape during the evolution due to the least amount of cancellation of $d\varepsilon/d\mathbf{k}$ during the evolution.

A more detailed characterization of the shape of the response surfaces can be performed by analyzing the high-symmetry directions. For instance, for the Hopf linked case, the constant A_0 surfaces look similar to ellipsoids [Figs. 6(b), 7(b), 7(f), and 7(j)] with the longest axis oriented along the 45° diagonal between the $J_x > 0$ and $J_z > 0$ axes, corresponding to the direction $\mathbf{J} \propto \pm(1, 0, 1)$. The three "principal axes" of the response surfaces are thus marked out by the three pairs of points $\pm(0, 1, 0)$, $\pm(1, 0, 1)$, and $\pm(1, 0 - 1)$, as discussed. [This is seen in Figs. 16(m)–16(p), where the magnitude for the responses along $\pm(1, 0, -1)$ is significantly smaller than along $\pm(1, 0, 1)$ and $\pm(0, 1, 0)$. This accounts for its oblate appearance.]

As we increase A_0 for the linked case, the two faces of the constant A_0 surface in Fig. 6(c) which are characterized by $\pm(1, 0, -1)$ exhibit concavity, reminiscent of the

Fermi surface	Small A_0	Intermediate A_0	Large A_0
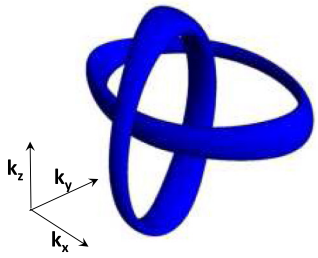	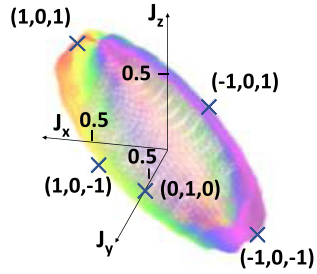	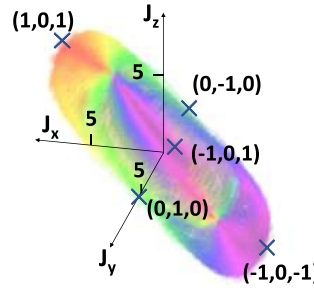	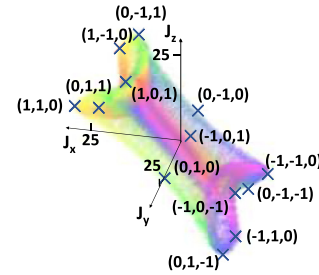
(a) $r_y = 0.6,\ r_x = 0.6,\ d = 0.15$	(b)	(c)	(d)
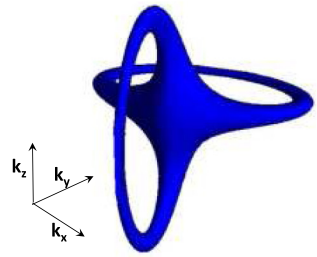	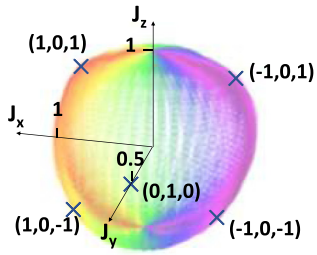	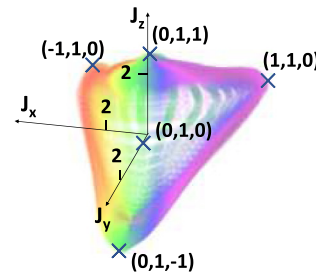	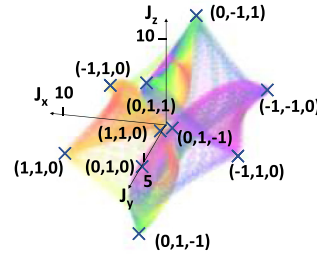
(e) $r_y = 0.6,\ r_x = 0.6,\ d = 0.6$	(f)	(g)	(h)
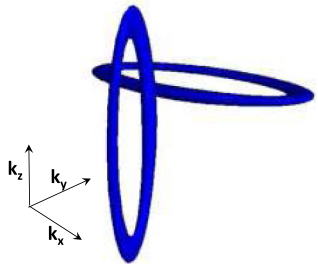	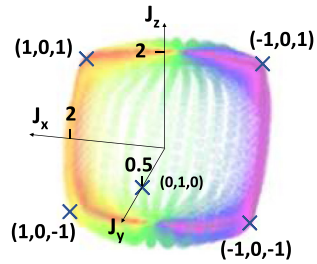	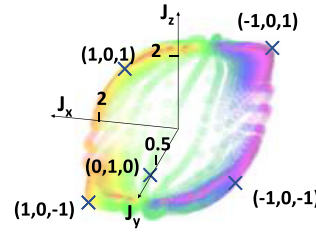	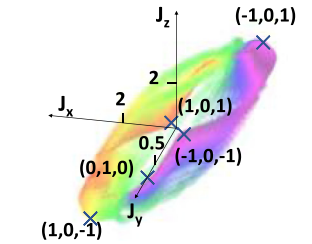
(i) $r_y = 0.6,\ r_x = 0.6,\ d = 1.3$	(j)	(k)	(l)

FIG. 6. For the three possible nodal configurations (linked, nodal chain, and unlinked) of our double-loop Hamiltonian, shown here are their corresponding surfaces $\mathcal{S}_J$ for constant chemical potential $\mu = 0.1$ under small, medium, and large impulses $A_0 = 0.1, 0.75, 1.75$ for the linked and chain cases and $A_0 = 0.1, 0.5, 1.0$ for the unlinked case. The qualitative evolution of the response surfaces with increasing A_0 differ for the different topological nodal configurations, with the large-A_0 response surface elongated towards the $J_z \pm J_x$ direction in the topologically linked and unlinked cases. (a)–(d) The response surfaces for the Hopf link $r_y = 0.6 > d = 0.15$, $r_x = 0.6$ exhibit concavity along directions $\pm(0, 1, 1)$, $(1, 0, \pm 1)$ due to the locally depressed responses in these directions. (e)–(h) The response surfaces for the nodal chain $r_y = 0.6 = d$, $r_x = 0.6$ do not obey the same symmetries as those in the Hopf link since the Fermi surface of the nodal chain breaks reflection symmetry. In particular, for intermediate A_0 values, the surface looks like a saddle with asymmetric responses; for example, $\hat{A} = (0, 1, 1)$ has a greater response than $\hat{A} = (0, -1, -1)$ at $A_0 = 0.75$. (i)–(l) The response surfaces for unlinked nodal rings $r_y = 0.6 > d = 0.15$, $r_x = 0.6$ respect these symmetries too but possess topologies distinct to the topologically linked case. The units of the response currents $\mathbf{J}$ are $10^{-3}\ env_F$, and parameters are chosen such that no periodic images are present.

shape of a red blood cell. [The concavity along the directions $\pm(1, 0, -1)$ can be better seen in Fig. 14(b), where the same response surface is viewed from a lateral direction.] This characteristic suppressed response is similar to that in Fig. 5(d), where it was a consequence of the nonmonotonicity of the response. In these cases, the responses along $\pm(1, 0, -1)$ increase significantly slower than in other directions [Figs. 16(m)–16(q)]. As A_0 continues to increase, the $\hat{A}$ directions characterized by $\pm(1, 0, 1)$ and $\pm(0, 1, 0)$ also exhibit concavity. Again, this is because the responses along $\pm(1, 1, 0)$, $\pm(0, 1 - 1)$, $\pm(0, 1, 1)$, $\pm(1, -1, 0)$ [which correspond to the eight corners of the surface in Fig. 6(d)] grow much quicker than along the principal directions [consistent with the individual response curves in Figs. 16(a)–16(l)]. This surface [Fig. 6(d)] also shows symmetry consistent with the symmetries in the responses [Figs. 16(a)–16(l)]. For instance, the constant A_0 surface has mirror symmetry about the $J_y = 0$ plane. Due to the non-negligible thickness of the

Fermi surface	$A_0 = 0.1$	$A_0 = 0.75$	$A_0 = 1.75$
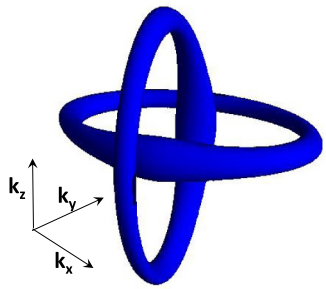	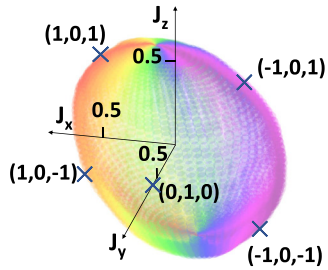	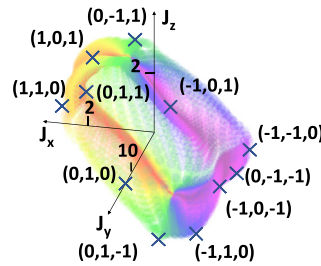	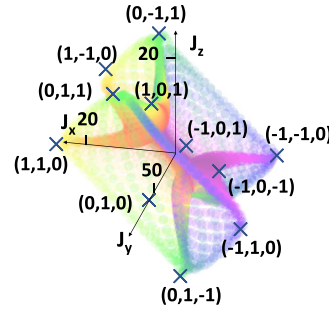
(a) $r_y = 0.4,\ r_x = 0.6,\ d = 0.15$	(b)	(c)	(d)
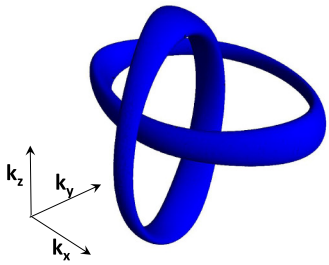	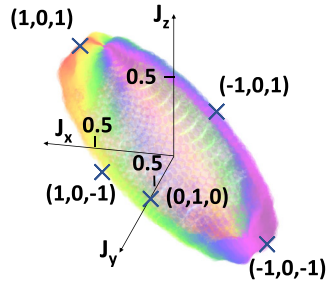	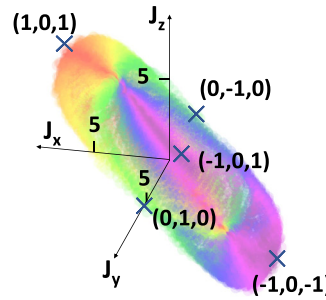	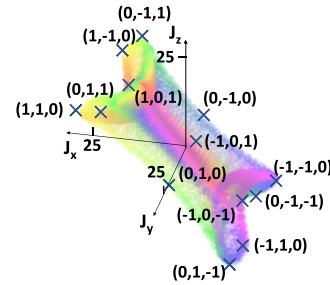
(e) $r_y = 0.6,\ r_x = 0.6,\ d = 0.15$	(f)	(g)	(h)
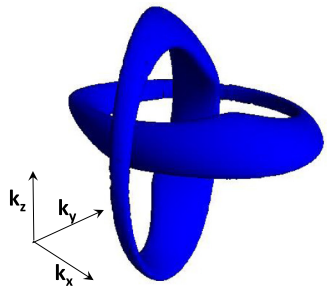	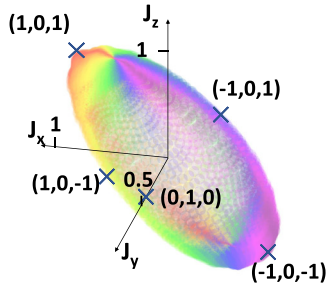	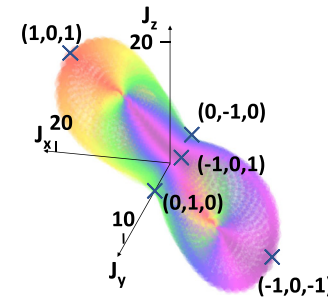	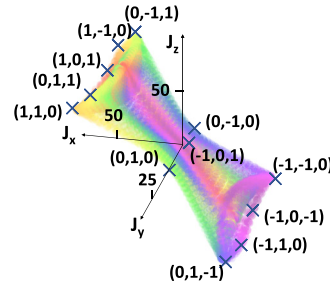
(i) $r_y = 0.6,\ r_x = 0.4,\ d = 0.3$	(j)	(k)	(l)

FIG. 7. The dependence of the surface morphologies on the aspect ratio parameters r_x, r_y of the nodal Hopf link at constant $\mu = 0.1$. Again, their response surfaces $\mathcal{S}_J$ are plotted for small, medium, and large impulses $A_0 = 0.1, 0.75, 1.75$, with current $\mathbf{J}$ in units of $10^{-3}\ env_F$. (a)–(d) The response surfaces for the Hopf link $r_y = 0.4 > d = 0.15$, $r_x = 0.6$. (e)–(h) The same response surfaces as in Figs. 6(a)–6(d). (i)–(l) The response surfaces for the Hopf link $r_y = 0.6 > d = 0.15$, $r_x = 0.4$ share several similarities with (e)–(h), but with a more depressed longitudinal response at $A_0 = 0.75$ and $A_0 = 1.75$ and a less depressed response along $\hat{A} = \pm(1, 0, 1)$ at $A_0 = 1.75$. Overall, the response surfaces differ for different geometric parameters but do not change as drastically as when the nodal topology changes (Fig. 6).

nodal loops, certain symmetries of the $\mu = 0$ nodal system may be broken. This symmetry breaking is particularly pronounced in the nodal chain case, where the two nodal rings intersect with relatively weak dispersion. Generically, the finitely thick nodal tube can break reflection symmetry in the direction of impulse; that is, translating the Fermi surface in the $+A_0\hat{y}$ direction results in a different response compared with doing so in the $-A_0\hat{y}$ direction. For small A_0, the surfaces are imperfectly rounded blobs [Fig. 6(f)] and evolve into a saddle shape [Fig. 6(g)] as A_0 grows. [This saddlelike shape is more obvious when viewed in a different orientation illustrated in Fig. 14(c).] It can be characterized by 6 out of the 14 points in total: (0,1,1), (1,1,0), $(0, \pm 1, 0)$, $(0, 1, -1)$, and $(-1, 1, 0)$. Again, we observe asymmetry in the sense that the responses grow more than proportionately in the directions (0,1,1), (1,1,0), $(0, 1, -1)$, and $(-1, 1, 0)$ (the negative pair does not grow as fast). As A_0 grow, so do the responses corresponding to the remaining eight points, giving rise to a surface such as that in Fig. 6(h), with six concave sides.

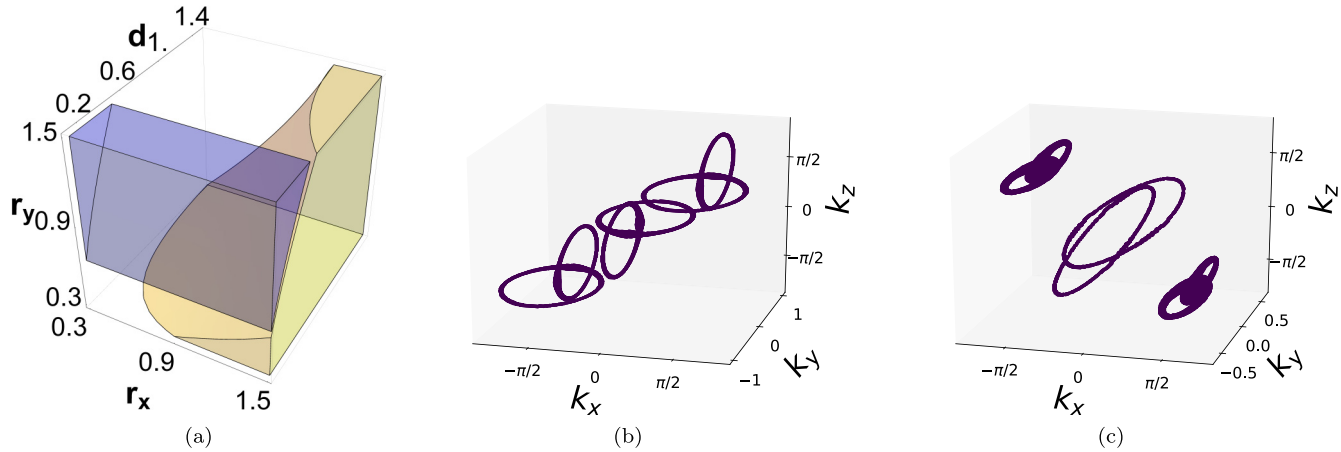

FIG. 8. (a) The regions in parameter space for the single Hopf structure (uncolored), type I periodic images (yellow), and type II periodic images (purple). (b) and (c) For nonvanishing μ, we illustrate the two types of periodic images which come in pairs in the first BZ. (b) The nodal loops of type I periodic images lie in the planes $(k_x = +\pi/2,\ k_z = +\pi/2)$ and $(k_x = -\pi/2,\ k_z = -\pi/2)$, as illustrated for the case $r_y = 0.6 > d = 0.4$, $r_x = 1.0$. (c) The nodal loops of type II periodic images lie in the planes $(k_x = -\pi/2, k_z = +\pi/2)$ and $(k_x = +\pi/2,\ k_z = -\pi/2)$, as illustrated for the case $r_y = 1.0 > d = 0.2$, $r_x = 0.8$.

For the unlinked nodal loops, the surface for small A_0 is again imperfectly rounded due to linear anisotropy. For intermediate A_0, the surface expands into a lemonlike shape due to the relatively small response nonlinearity and can be characterized by the surface directions $\pm(1, 1, 0)$, $\pm(0, 1, 1)$, and $\pm(1, -1, 0)$. As A_0 grow, the responses in the $\pm(1, 0, 1)$ directions do not grow as fast, and thus the face characterized by this pair of points exhibits concavity. For large A_0, the response surface elongates towards the $J_z - J_x$ direction, which differs from the linked case, where it elongates towards the $J_z + J_x$ direction. This conclusively relates the response surfaces with the topological linkage of the nodal loops.

B. Response surfaces and nodal geometry

Since the nonlinear response current does not correspond to any topologically quantized value, we expect it to be affected by deformations of the nodal structure too. This should

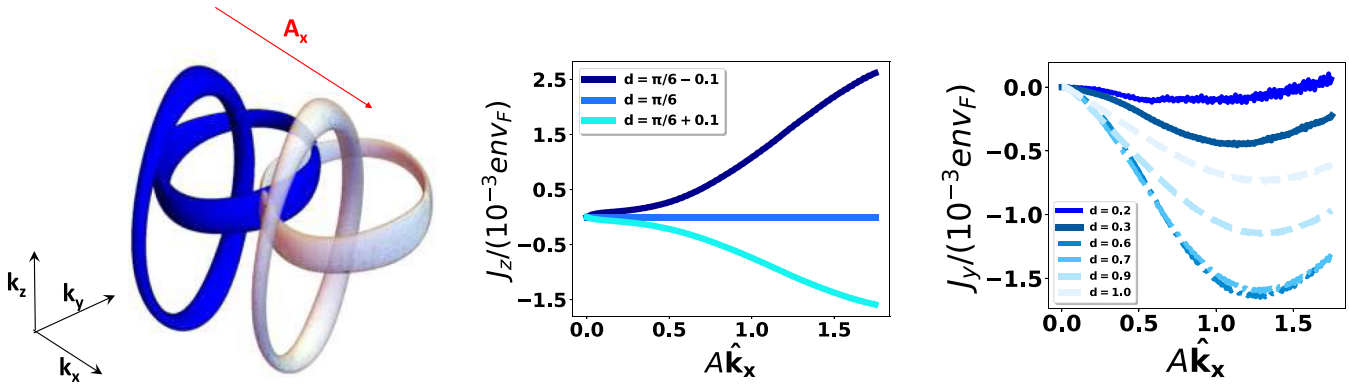

FIG. 9. (a) In the presence of an applied transverse field $A\hat{x}$, the Fermi surface of the Hopf link is displaced along the transverse k_x axis in **k** space. On top of the diagonal responses, we obtain additional Hall responses, which exhibit trends that are not related to the topological linkage of the nodal rings. (b) When the intermediate parameter ξ in the Hamiltonian [Eq. (3)] is set to 1, the transverse Hall response will vanish for all values of impulse $A(t) = e\int_{-\infty}^{t} E(t')dt'$. For the case of circular nodal loops $r_x = r_y$, the corresponding critical d value is $d_{\text{crit}} = \pi/6$. In the plot, we chose $r_x = r_y = 0.6$ and $\mu = 0.1$ such that the nodal tubes are thick enough to give nodal chains even when $d = \pi/6 < r_y$. Yet, even as the nodal loops touch each other, the transverse Hall response still vanishes when $d = d_{\text{crit}}$. This demonstrates that the topological linkage of the nodal loops is not important for this response. (c) Comparing the longitudinal transverse Hall responses for the Hopf link (solid lines, $d = 0.2, 0.3$), unlinked nodal loops (dashed lines, $d = 0.9$, $d = 1.0$), and the nodal chain (dash-dotted lines, $d = 0.4, d = 0.8$) for $r_y = 0.6 = r_x$. The response increases in magnitude with d and exhibits the largest magnitude when the nodal loops touch each other. For the Hopf link, this response is extremely weak at small fields and increases as we increase the field strength A. Here, there is no distinct difference between the topologically trivial case and the topologically linked case, but rather a smooth continuous change with d. (b) and (c) The responses are in units of $envF$, where n and v_F are the electronic number density and Fermi velocity of the NLSM material, respectively.

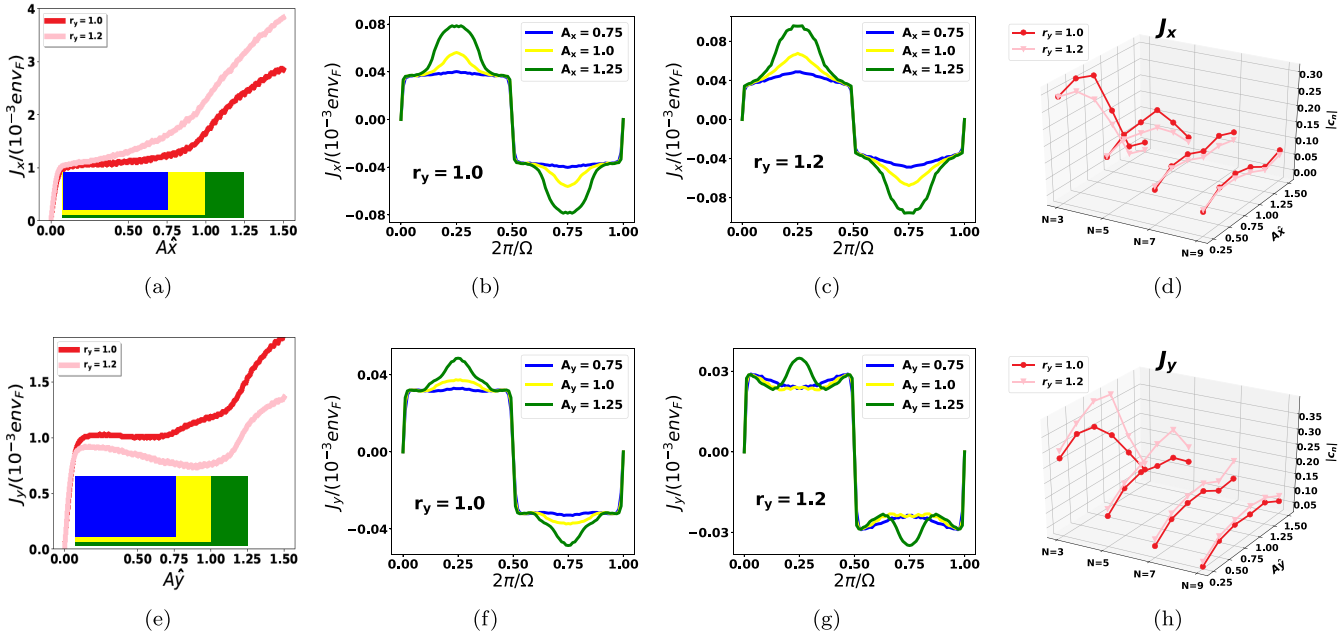

FIG. 10. To demonstrate the anisotropic response of the Hopf link, we compare its transverse and longitudinal diagonal responses for the parameters $r_x = 1$, $d = 0.6 < r_y = 1.0, 1.2$. (b), (c), (f), and (g) demonstrate how the response curves distort sinusoidal signals of different amplitudes $A = 0.75, 1.0, 1.25$ near the turning point of the responses (as indicated by the corresponding colored regions in the response curves) for $r_y = 1.0$ and $r_y = 1.2$, respectively. (a)–(d) We compare the extent of nonlinearity of the transverse diagonal response J_x $(A\hat{x})$ for $r_y = 1.0, 1.2$. In (a), the response for $r_y = 1.0$ is clearly more nonlinear. (b) and (c) The sinusoidal signal for $r_y = 1.0$ experiences slightly more distortion. The greater nonlinearity is confirmed in (d), where the HHG coefficients $|c_n|$ are consistently larger for $r_y = 1.0$. (e)–(h) Similarly, we compare the extent of nonlinearity of the longitudinal diagonal response J_y (A_y). In (e), the response for $r_y = 1.2$ is instead more nonlinear. (f) and (g) The sinusoidal signal for $r_y = 1.2$ acquires additional fluctuations of higher frequency. This is confirmed in (h), where the HHG coefficients $|c_n|$ are drastically larger for $r_y = 1.2$, especially at the turning point $A_y = 1.0$.

apply to both linked and unlinked cases, even if the linked case is more likely to possess a strongly nonlinear response. Earlier, we have considered circular nodal loops with $r_x = r_y$. How will the surfaces in Fig. 6 change as we vary r_y and r_x? Varying r_y and r_x adds one more layer of complexity in our analysis of these surfaces. To study that, we shall start from the parameters in Figs. 6(a)–6(c) and change r_y and r_x separately, as presented in Fig. 7.

Generally, the surfaces along the same column of Fig. 7 will have relatively similar morphologies since they are only slightly distorted from each other and correspond to the same A_0 impulse. In particular, the special symmetries in Figs. 6(b)–6(d) are no longer satisfied as the relative responses along the various directions now behave quite differently. This occurs because a chemical potential of $\mu = 0.1$ results in nodal loops with significantly nonuniform and asymmetric thickness [Fig. 7(i)]. This further enhances the anisotropy of the response surfaces, particularly at $A_0 = 0.75$. However, at high fields $A_0 = 1.75$, the surface morphologies of Figs. 7(d) and 7(h) share similar morphological features—suppressed response at $\pm(1, 0, 1)$ and $\pm(1, 0, -1)$. Again, this anisotropic response is due to the varying rates of growth for the responses

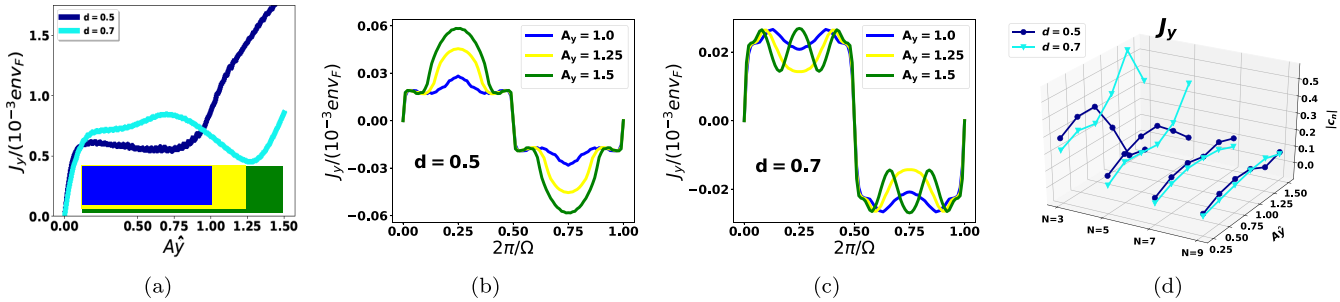

FIG. 11. To demonstrate the enhanced nonlinearity of the longitudinal diagonal response of the Hopf link, we compare $d = 0.5, 0.7$ for the parameters $r_x = 0.6$, $r_y = 1.0 > d$. In (a), the response for $d = 0.7$ is clearly more nonlinear. (b) and (c) demonstrate how the response curves distort sinusoidal signals of different amplitudes $A = 1.0, 1.25, 1.5$ near the turning point of the responses (as indicated by the corresponding colored regions in the response curves) for $d = 0.5$ and $d = 0.7$, respectively. The sinusoidal signal for the latter acquires additional fluctuations of higher frequency and thus appears significantly distorted. The greater nonlinearity for $d = 0.7$ is confirmed in (d), where the HHG coefficients $|c_n|$ are drastically higher for $d = 0.7$ at the turning points of the response curves.

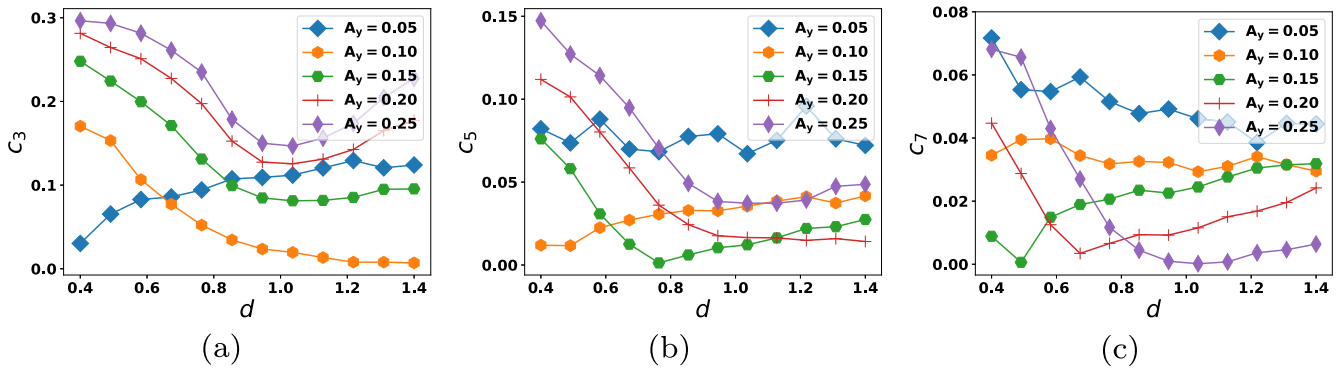

FIG. 12. For the parameters $r_x = 0.9$, $r_y = 1.1$ and $\mu = 0.1$, we plot the HHG coefficients $|c_n|$ against the loop separation d for various small longitudinal fields A_y, and $n = 3, 5, 7$. The HHG coefficients are consistently higher in the $d < r_y$ regime, i.e. topologically linked.

along the individual directions. For instance, $\pm(1, 0, 1)$ does not grow as fast as, say, $\pm(1, 1, 0)$ in Fig. 7(h) but grows at comparable rates in Fig. 7(l).

V. CONCLUSION

In this paper, we have systematically studied in detail the anisotropic and nonlinear optical response of two nodal loops that are linked, unlinked, or touching (nodal chain). This system, as parametrized by our canonical two-nodal-loop model, represents the simplest abstraction of simultaneously occurring nodal loops (linked or unlinked) in nodal materials. First, we studied the effects of nodal geometry and topology individually along various axis directions. Next, we presented constant A_0 response surfaces to highlight the anisotropy of the response and how that global picture can shed light on the overall configuration of the nodal structure. Our findings generalize existing results on the enhancement of optical response nonlinearity by nodal linkages [95] to various transverse, Hall, and diagonal sectors and introduce a geometric picture of response nonlinearity and anisotropy that will be invaluable in analyzing generic nodal material responses, as well as the engineering of high-order-harmonic generation materials for applications such as terahertz radiation generation.

ACKNOWLEDGMENTS

T.T. is supported by the National Science Scholarship from A*STAR of Singapore. This work was supported by a Singapore Ministry of Education (MOE) Tier 1 start-up grant (Grant No. R-144-000-435-133).

APPENDIX A: PERIODIC IMAGES OF THE NODAL HAMILTONIAN

Periodic images occur when there is more than one branch of solution (usually three in total) when we solve $h = 0$ and $g = 0$ simultaneously in the Hamiltonian $H_{\text{Hopf}}(\mathbf{k}) = h(\mathbf{k})\sigma_x + g(\mathbf{k})\sigma_y$, as defined in Eqs. (4a) and (4b) of the main text. We can deduce their positions from the k_z planes the periodic images lie in, as well as the k_x lines these periodic images are symmetrical with respect to. There are two types of periodic images, both of which occur in pairs. We distinguish them based on their positions:

(*i*) *Type I*. The pair of images have their loops lie in the planes $(k_x = +\pi/2, k_z = +\pi/2)$ and $(k_x = -\pi/2, k_z = -\pi/2)$, respectively [Fig. 8(b)].

(*ii*) *Type II*. The pair of images have their loops lie in the planes $(k_x = +\pi/2, k_z = -\pi/2)$ and $(k_x = -\pi/2, k_z = \pi/2)$, respectively [Fig. 8(c)].

Only the single Hopf regime [uncolored in Fig. 8(a)] is studied in detail in this paper, since it provides the most conclusive results on how the nodal shape and topological linkage affect transport properties.

Trivially, $g = 0$ in both types of constraints, and we only need to solve for $h = 0$ to obtain the explicit form of the

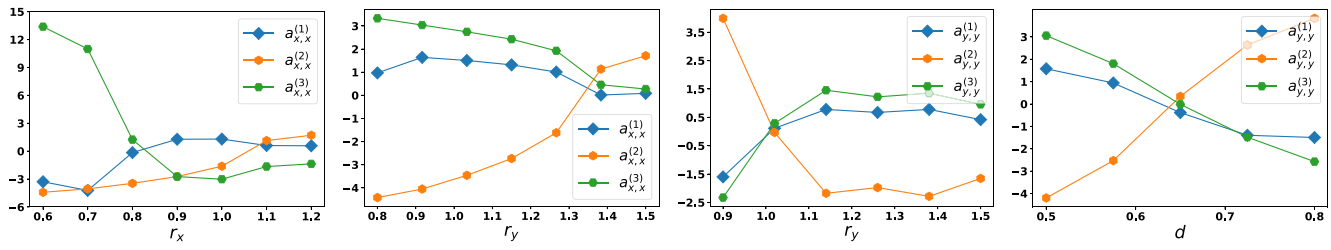

FIG. 13. (a) and (b) The expansion coefficients $a^{(i)}_{xx}$, $i = 1, 2, 3$, were plotted with r_x (a) and r_y (b) for the parameters $r_y = 1.0$, $d = 0.5$ and $r_x = 1.0$, $d = 0.5$, respectively. The parameters chosen are identical to the transverse diagonal response $J_x(A\hat{x})$ in Fig. 3. (c) and (d) The expansion coefficients $a^{(i)}_{yy}$, $i = 1, 2, 3$, were plotted with r_y (c) and d (d) for the parameters $r_y = 1.0$, $r_x = 0.6$ and $r_x = 1.0$, $d = 0.6$. The parameters chosen are identical to the longitudinal diagonal response $J_y(A\hat{y})$ in Fig. 4.

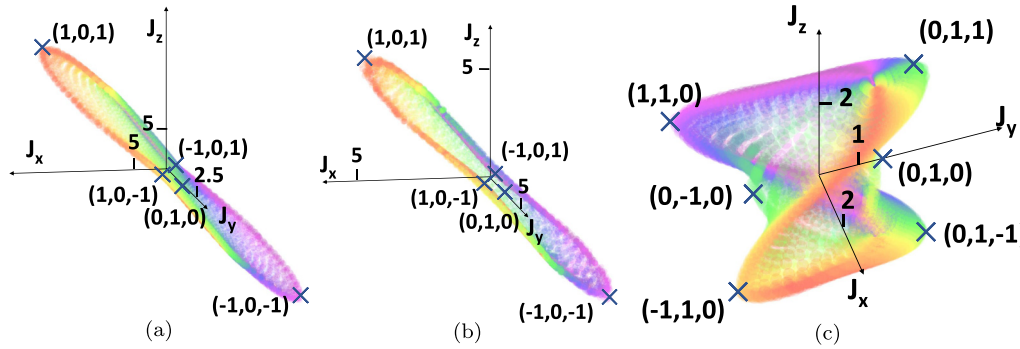

FIG. 14. For three particular surfaces, shown in Figs. 7(k), 6(c), and 6(g), we present a viewpoint that is different from the previous standardized orientation. This new viewpoint was chosen to highlight the key features of these response surfaces, namely, (a) and (b) the concavity along the directions $\hat{A} = \pm(1, 0, -1)$, which characterizes its red-blood-cell-like appearance, as well as (c) the overall saddle-shaped appearance. The units of $\mathbf{J}$ are in 10^{-3}env_F.

periodic images. For type I images, we have

$$\alpha \sin k_y = \pm(\beta \cos k_y + \gamma), \tag{A1}$$

where $\alpha = (\cos r_x - 1)$, $\beta = -(\cos r_x - 1)\cot d$, and $\gamma = 2 + \text{cosec}\, d(-2 + \cos r_y) + \cos r_x(\cos r_y \,\text{cosec}\, d - 2)$. Equation (A1) can be solved as follows:

$$\sqrt{\alpha^2+\beta^2}\sin(k_y \mp \delta) = \pm\gamma \Rightarrow$$
$$k_y = \sin^{-1}\left(\pm\frac{\gamma}{\sqrt{\alpha^2+\beta^2}}\right) \pm \tan^{-1}\frac{\beta}{\alpha}, \tag{A2}$$

where $\frac{\gamma}{\sqrt{\alpha^2+\beta^2}} = \frac{\gamma \sin d}{\cos r_x - 1}$, $\frac{\beta}{\alpha} = -\cot d$. Type I periodic images arise when there exist real solutions for Eq. (A2). This implicitly requires the argument in the inverse sine in Eq. (A2) to have magnitude less than 1. In other words, the criteria for type I periodic images are given as the following inequality:

$$\frac{-2 + \cos r_y(1 + \cos r_x)}{\cos r_x - 1} - 2\sin d \leqslant 1. \tag{A3}$$

Type II images arise from another solution branch described by a quadratic equation in $\cos k_y$, which gives the solution

$$\cos k_y = \frac{1}{2}\sin^2 d((4 + 2\cos r_y)\cot d\,\text{cosec}\, d \pm \sqrt{-12 + 4\cot^2 d - 16\cos r_y \text{cosec} d - 4\cos^2 r_y \text{cosec}^2 d}). \tag{A4}$$

The corresponding regime for the type II image is set by the above discriminant (the argument in the square-root term) being strictly positive, i.e.,

$$-12 + 4\cot^2 d - 16\cos r_y \text{cosec} d - 4\cos^2 r_y \text{cosec}^2 d > 0. \tag{A5}$$

APPENDIX B: NONDIAGONAL RESPONSES ALONG THE PRINCIPAL DIRECTIONS

There are a total of four distinct responses along the principal directions in Eq. (6), where the diagonal responses are accounted for in detail in Sec. III. The remaining two responses are nondiagonal (Hall responses) and are distinguished with respect to the direction of the loop separation, i.e., transverse Hall response $J_z(A\hat{x})$ and longitudinal transverse Hall response $J_y(A\hat{x})$. As we will show, these responses are specific to the chosen form of the Hamiltonian and are not related to the topological linkage of the nodal loops.

When we set the intermediate parameter $\xi = \frac{\cos r_y - 1}{\cos r_x - 1}\frac{1}{\sin d} - 1$ in the Hamiltonian [Eq. (3)] as 1, the functions $h(\mathbf{k})$ and $g(\mathbf{k})$ [Eqs. (4a) and (4b)] are even and odd under the inversion $\mathbf{k} = (k_x, k_y, k_z) \to (-k_x, k_y, -k_z)$. This symmetry results in a vanishing transverse Hall response for all values of impulse A. In another words, there exists a critical value of d, d_{crit}, that satisfies $\xi = 1$ and is given as

$$d_{\text{crit}} = \sin^{-1}\frac{\cos r_y - 1}{2(\cos r_x - 1)}. \tag{B1}$$

When such solutions for d_{crit} exist, then the sign of the response will be $\text{sgn}(d - d_{\text{crit}})$. This remains true even if the nodal loops are no longer linked, i.e., $d_{\text{crit}} > r_y$. In Fig. 9(b), we considered the simple example of circular nodal loops where $r_y = r_x$; then Eq. (B1) gives $d_{\text{crit}} = \frac{\pi}{6}$. In the particular example where $\mu = 0.1$ and $r_x = r_y = 0.6 > d_{\text{crit}} = \frac{\pi}{6}$, the nodal tubes are sufficiently thick to have the nodal loops of the Hopf link touch each other, giving an accidental nodal chain instead. As we can see, the topological linkage of the nodal loops is not important in this response.

The longitudinal transverse Hall response increases in magnitude with d and attains the largest possible magnitude when the nodal loops touch each other. This is illustrated in Fig. 9(b), where we again consider $r_y = r_x = 0.6$. We see that when $d = 0.2, 0.3 < r_y$, the response of the Hopf link is significantly weaker, but nonvanishing at small fields. This response grows with d and is the largest when the nodal loops touch each other, $d = 0.6, 0.7 \sim r_y$. As for the unlinked case, this response is weaker than that of the nodal chain and stronger than that of the Hopf link. The response thus has no

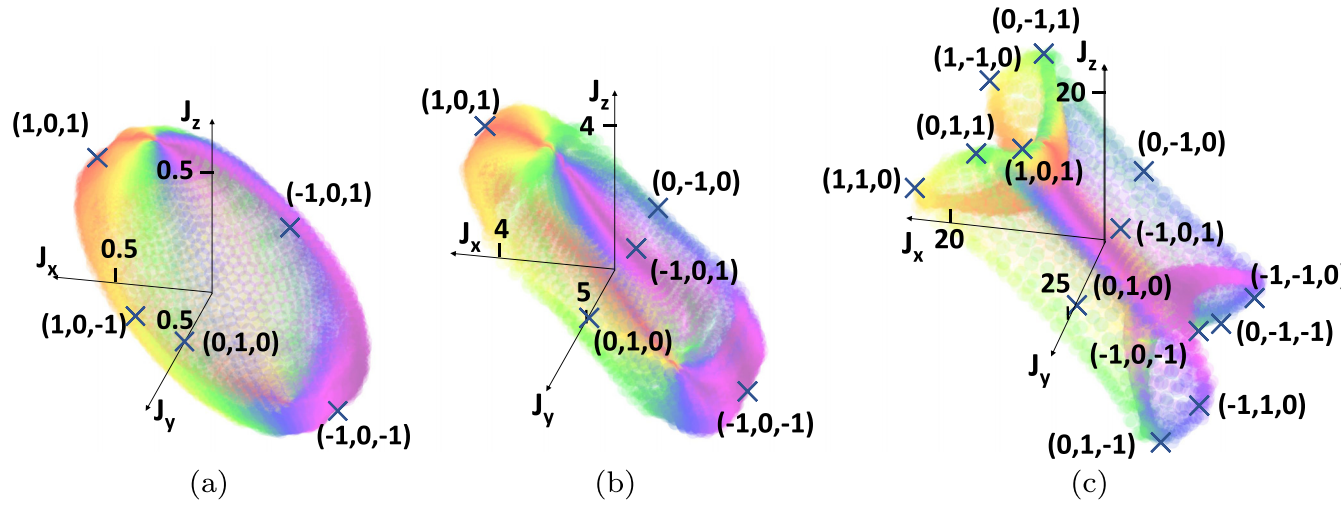

FIG. 15. When the loop aspect ratio $\frac{r_x}{r_y}$ is only slightly greater than unity, the response surfaces are similar to that in Fig. 7(f)–7(h) in terms of morphology, showing little deviation. (a-c) The response surfaces for the Hopf link $r_y = 0.5 > d = 0.15$, $r_x = 0.6$ for small, medium and large impulses $A_0 = 0.1, 0.75, 1.75$. The units of $\mathbf{J}$ are in 10^{-3}env_F.

significant contrast between the topologically linked case and the trivial case, but rather it varies smoothly with d.

APPENDIX C: NONLINEAR AND ANISOTROPIC RESPONSE OF THE HOPF LINK IN TERMS OF HHG

For an oscillatory electric field of frequency Ω, the potential amplitude $A = E/\Omega$ is related to the external field amplitude E. To quantify the nonlinearity of the response expansion, we can do a vectorial perturbative expansion for the response about the point $\mathbf{A_0}$ up to second order, which is valid in the perturbative regime, i.e., for sufficiently small A_0:

$$\begin{aligned} J_i(\mathbf{A}) - J_i(\mathbf{A_0}) &= \sum_{j=x,y,z} \left.\frac{\partial J_i}{\partial A_j}\right|_{\mathbf{A_0}} (\mathbf{A}-\mathbf{A_0})\cdot\hat{j} \\ &\quad + \frac{1}{2}\sum_{j,k=x,y,z} \left.\frac{\partial^2 J_i}{\partial A_j \partial A_k}\right|_{\mathbf{A_0}} \\ &\quad \times (\mathbf{A}-\mathbf{A_0})\cdot\hat{j}\,(\mathbf{A}-\mathbf{A_0})\cdot\hat{k} + \cdots \\ &= \sum_{j=x,y,z} a_{ij}\Delta\mathbf{A}\cdot\hat{j} \\ &\quad + \frac{1}{2}\sum_{j,k=x,y,z} a_{ijk}\Delta\mathbf{A}\cdot\hat{j}\,\Delta\mathbf{A}\cdot\hat{k} + \cdots, \end{aligned} \tag{C1}$$

where we defined the expansion coefficients as the partial derivatives in the expansion, for instance,

$$a_{ij} = \left.\frac{\partial J_i}{\partial A_j}\right|_{\mathbf{A_0}}, \quad a_{ijk} = \left.\frac{\partial^2 J_i}{\partial A_j \partial A_k}\right|_{\mathbf{A_0}}, \tag{C2}$$

which can be approximated using the finite difference method for a small perturbation $|\Delta\mathbf{A}| = |\mathbf{A} - \mathbf{A_0}|$. These coefficients are related to the conductivities or susceptibilities familiar in optical materials and are of experimental interest. The evolution of the response surface with the field strength A_0 may thus be reconstructed once all the expansion coefficients are determined. For a given field strength A_0 and direction $\frac{\mathbf{A_0}}{A_0}$, the 18 unique coefficients a_{ijk} quantify the lowest-order nonlinearity of the responses (the mixed partial derivatives are symmetrical).

Unfortunately, these expansion coefficients alone display limited information since they are local properties of the response manifold and only contain geometric information around their chosen field directions and magnitudes. Combined with our response surface picture, the topology and geometry of the overall response behavior are given a clearer global picture.

To understand the coefficients a_{ijk}, we consider the simple case of $j = k$. Consider $\mathbf{A}$ along a particular direction (in general, higher-order response coefficients involve more than one component of $\mathbf{A}$), e.g., the principal directions, so we may simply fit the optical response J with a simple polynomial in A:

$$J_i(\mathbf{A}\cdot\hat{j}) = a_{i,j}^{(0)} + a_{i,j}^{(1)}A + a_{i,j}^{(2)}A^2 + a_{i,j}^{(3)}A^3 + \cdots. \tag{C3}$$

The coefficients $a_{i,j}^{(r>1)}$ quantify the response's nonlinearity. Take the example $r_x = 1$, $d = 0.6 < r_y = 1.0, 1.2$ [diagonal response curves given in Figs. 10(a) and 10(e)]; the response curves are linear in the small field regime $0 < A < 0.1$ and cubic in the intermediate field regime $0.1 < A < 1.2$. For the cubic regime, the coefficients are

$$a_{x,x}^{(1)} = 0.6935, \quad a_{x,x}^{(2)} = -0.905\,31, \quad a_{x,x}^{(3)} = 1.478\,78, \tag{C4a}$$

$$a_{y,y}^{(1)} = 0.751\,34, \quad a_{y,y}^{(2)} = -2.130\,35, \quad a_{y,y}^{(3)} = 1.311\,72. \tag{C4b}$$

The drastic difference in $a^{(2)}$'s shows that the longitudinal diagonal response $J_y(A\hat{y})$ is significantly more nonlinear than the transverse diagonal response $J_x(A\hat{x})$; hence the optical response is anisotropic. Another way to quantify the nonlinearity of the response is the high-order-harmonic generation

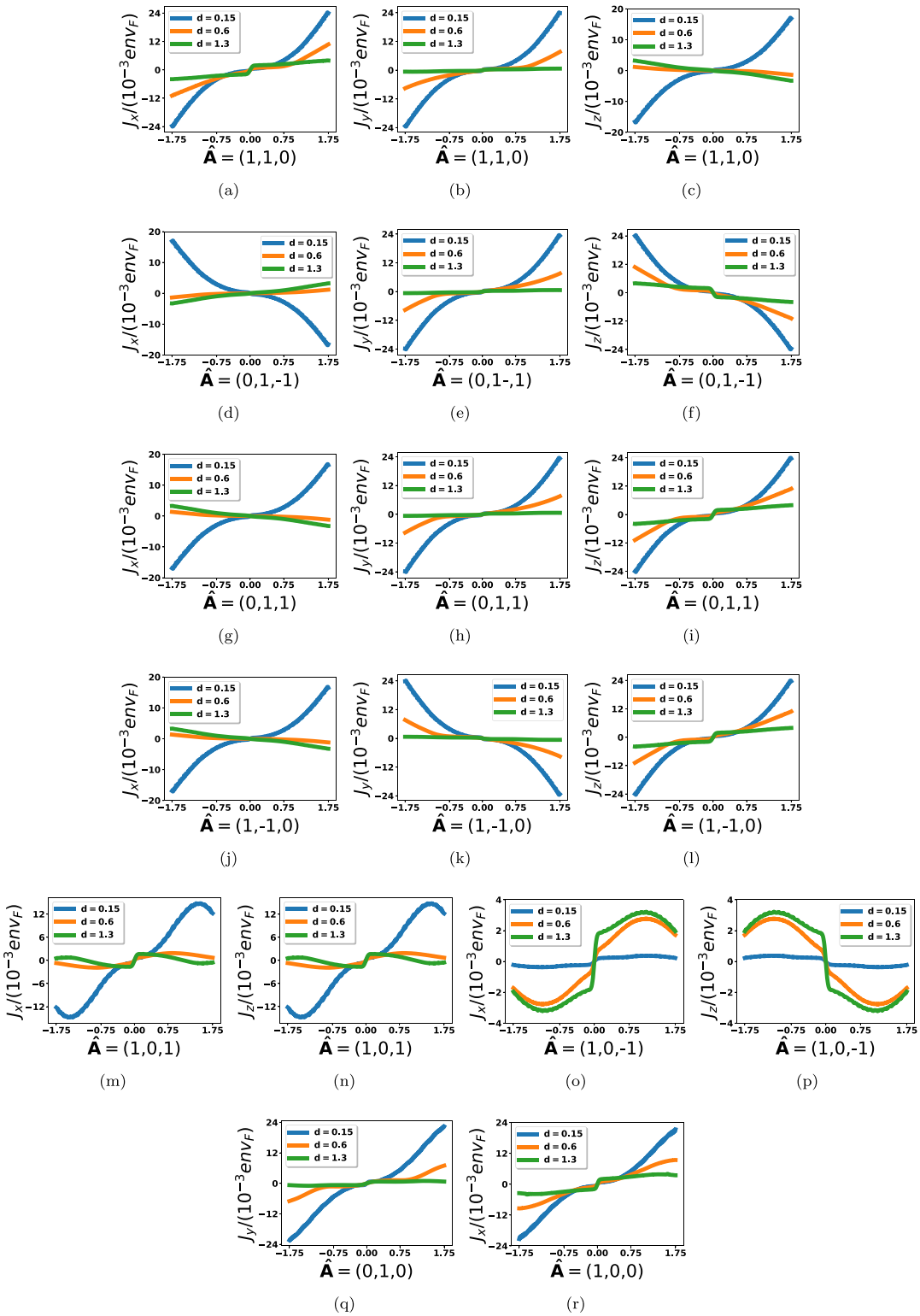

FIG. 16. The evolution with field strength of the diagonal responses, as well as the responses along the high-symmetry directions that fully characterize the response surfaces in Fig. 6 for the Hopf link $d = 0.15 < r_y$, the nodal chain $d = 0.6 = r_y$, and the unlinked case $d = 1.3 > r_y$.

(HHG) coefficients $c_n \sim |J(n\Omega)|/|J(\Omega)|$; that is, the greater the nonlinearity, the larger the HHG coefficients, which is experimentally measured by the extent of distortion for a sinusoidal signal. Under a sinusoidal signal, we can always expand the response as a superposition of high-order-harmonic signals, i.e.,

$$J_i[A_j(t)] = J_i(A_{j,0}\sin\Omega t) \propto \sin\Omega t + \sum_{n>1} c_n \sin\Omega t. \tag{C5}$$

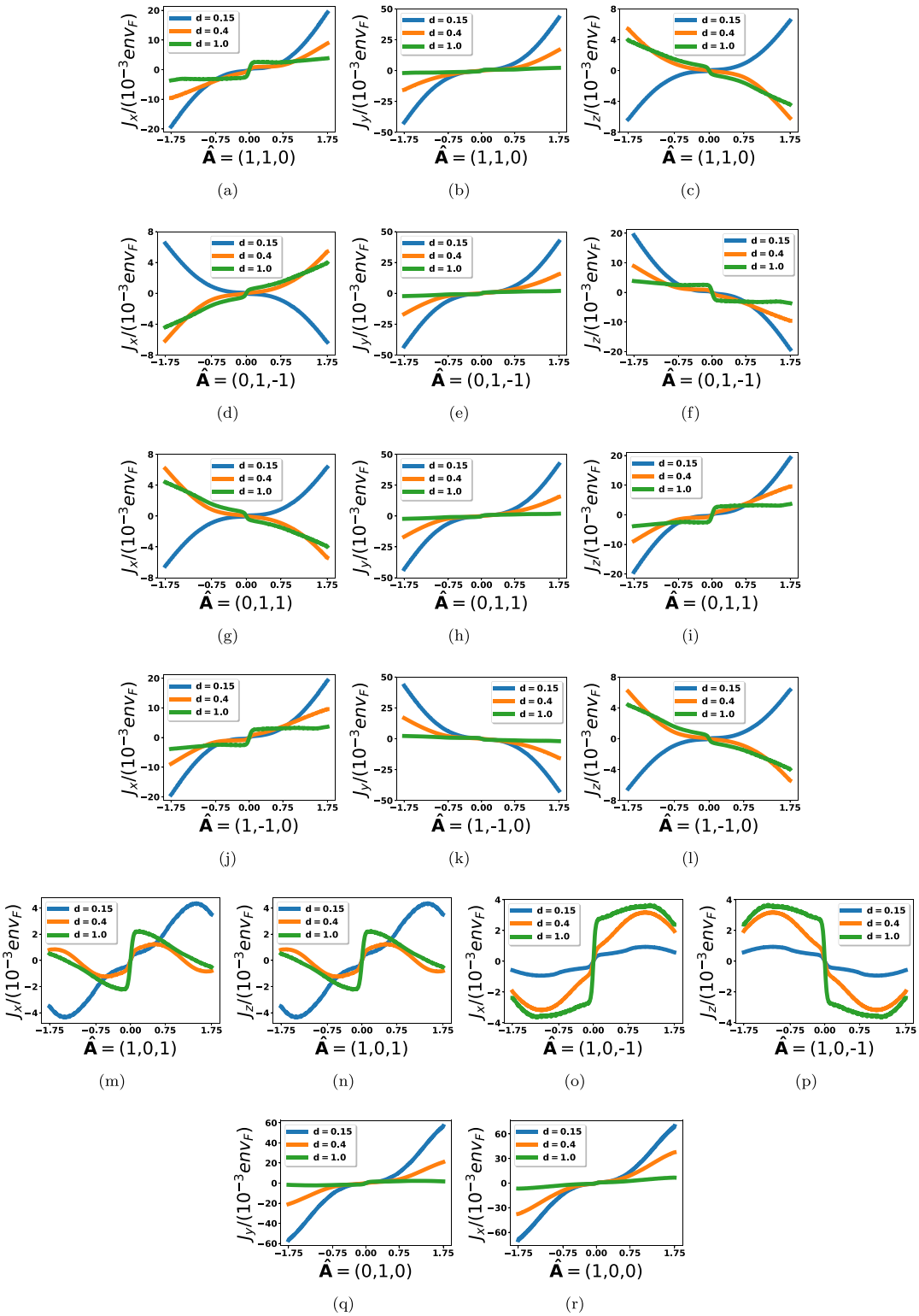

FIG. 17. The evolution with field strength of the diagonal responses, as well as the responses along the high-symmetry directions that fully characterize the response surfaces in Figs. 7(b)–7(d). Although we showed only the response surfaces for the Hopf link in Fig. 7, we have also included the responses for the nodal chain case $d = 0.6 = r_y$ and the unlinked case $d = 1.2 > r_y$.

For the same example, we compare the HHG coefficients of the transverse and longitudinal diagonal responses. $r_y = 1.0$ indeed shows smaller and larger HHG coefficients [Figs. 10(d) and 10(h)] in the longitudinal and the transverse directions, respectively. The resulting distortion to an arbitrary sinusoidal signal is more apparent in the former. Considering another example, increasing the loop separation d greatly increases the nonlinearity of the longitudinal diagonal response curve and thus leads to enhanced HHG (Fig. 11). This is manifested as a larger kink in the response curves [similar to Fig. 4(b)]

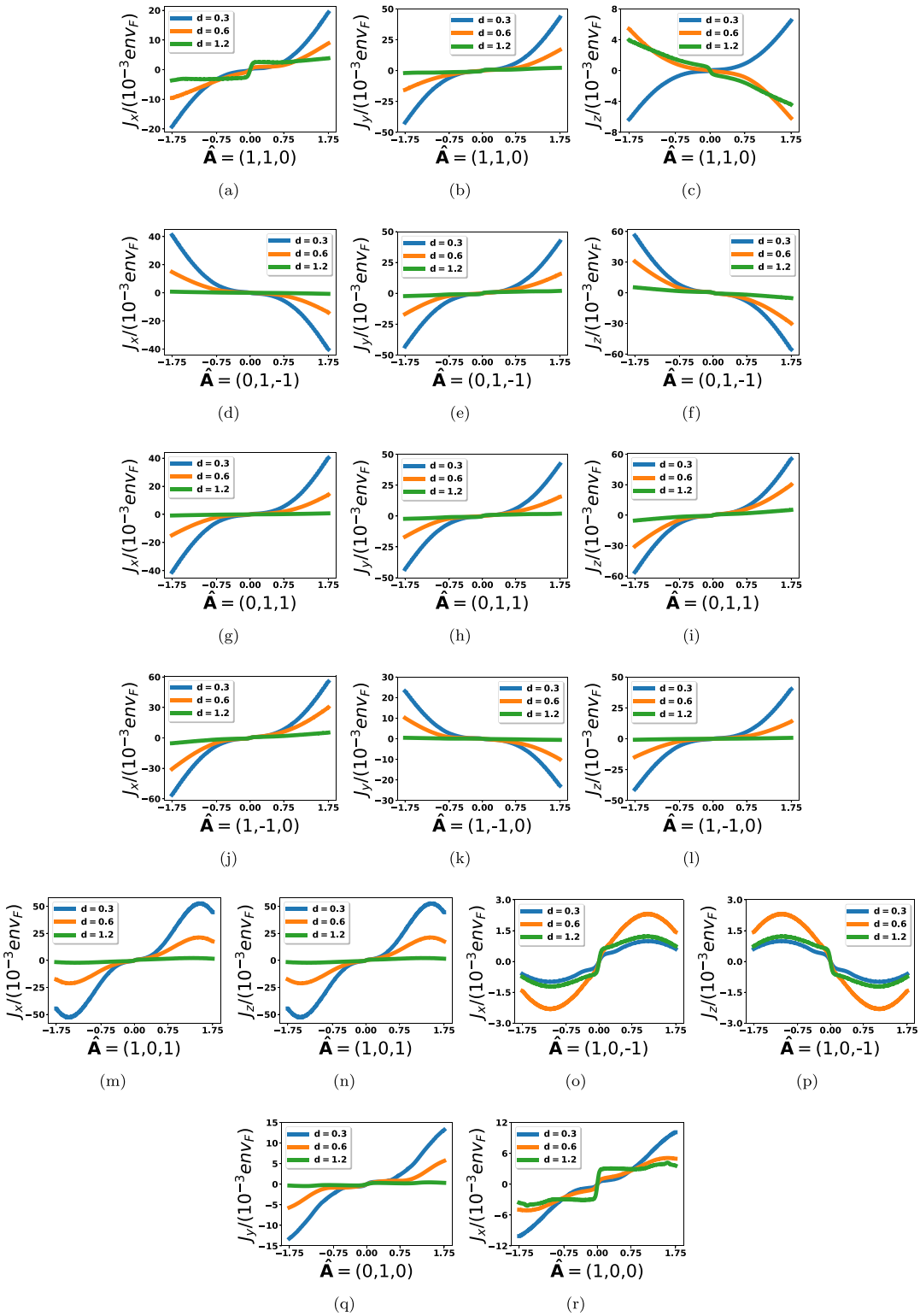

FIG. 18. The evolution with field strength of the diagonal responses, as well as the responses along the high-symmetry directions that fully characterize the response surfaces in Figs. 7(j)–7(l). Although we showed only the response surfaces for the Hopf link in Fig. 7, we have also included the responses for the nodal chain case $d = 0.4 = r_y$ and the unlinked case $d = 1.0 > r_y$.

and thus significantly more distortion to the sinusoidal signal.

Finally, since the longitudinal diagonal response is distinctly more nonlinear when the loops are topologically linked, we thus see enhanced HHG in the topologically linked regime (Fig. 12). This is consistent with Ref. [95], which demonstrates that real materials with topologically linked nodal loops exhibit higher HHG compared with materials with only a single nodal loop.

The expansion coefficients $a_{i,j}^{(k>1)}$ in Eqs. (C4a) and (C4b) also vary with the loop parameters r_x, r_y, d, adding one more layer of complexity to the response of nodal link semimetals (NLSMs). Up to intermediate fields of $A \lesssim 1.2$, the perturbative expansion equation (C3) remains valid. The expansion coefficients of the transverse diagonal response $J_x(A\hat{x})$ in Figs. 3(c) and 3(d) were plotted with the variation of r_x and r_y in Figs. 13(a) and 13(b), respectively. Similarly, for the longitudinal diagonal response $J_y(A\hat{y})$ in Figs. 4(b) and 4(d), the expansion coefficients were plotted with the variation of r_y and d in Figs. 13(c) and 13(d), respectively. We can immediately see that the nonlinearity of the responses evolves differently in the longitudinal and transverse directions, hinting at anisotropic behavior in the response of NLSMs.

This anisotropic behavior is, however, the tip of the iceberg. Given further that $\mathbf{J}(\mathbf{A_1} + \mathbf{A_2}) \neq \mathbf{J}(\mathbf{A_1}) + \mathbf{J}(\mathbf{A_2})$, the global anisotropy picture cannot be sufficiently illustrated via perturbative expansion plots such as those in Fig. 13. This thus brings us to the response surface illustration, as elaborated in Sec. IV and supplemented in Appendix D.

APPENDIX D: DETAILED STUDY OF THE ANISOTROPY

In Sec. IV, we demonstrated the evolution of the response surface with field strength. This encapsulates the full information about the response anisotropy and nonlinearity, and to some extent the nodal structure and its dispersion. In Figs. 6 and 7, we illustrated the surface using a common viewpoint to demonstrate this evolution with field strength. Yet this is not always the best orientation to understand the important characteristics of these surfaces. A locally suppressed response when viewed away from the observer will not be seen in this standard orientation.

For instance, in Figs. 7(g) and 7(k), it is not immediately obvious that these surfaces are indeed reminiscent of the shape of a red blood cell. In Figs. 14 and 15, we better illustrate the distinctive concave shapes that characterize a red blood cell appearance by explicitly demonstrating the concavity along the directions $\hat{A} = \pm(1, 0, -1)$. In addition, we clearly highlight the saddle-shaped appearance [which is not made obvious in Fig. 6(g)] by choosing a better orientation in Fig. 14. Here, we can more clearly see that the responses along the directions $\hat{A} = (0, 1, 1), (1, 1, 0), (0, 1, -1), (-1, 1, 0)$ are indeed asymmetric as they demonstrate a stronger growth along a preferred sense.

In Fig. 7, the response surfaces appear distinct when the loop aspect ratio $\frac{r_x}{r_y}$ is greater than unity. But when the loop aspect ratio is only slightly greater than unity, the response surfaces (Fig. 15) look almost similar to that in Fig. 7(f)–7(h), with only slight variation. It thus shows that there is a greater morphology variation when we increase the loop aspect ratio.

Finally, only snapshots of the response surfaces at particular A_0 values were chosen in Figs. 6 and 7. This, however, does not capture the full evolution of these surfaces with field strength. Since the diagonal responses and the responses along the high-symmetry directions [namely, $\hat{A} = (1, \pm1, 0), (0, 1, \pm1), (1, 0, \pm1)$] were shown to be useful in identifying key features of the response surface, we thus show these individual response curves (Figs. 16–18) for the corresponding surfaces. The relative rates of growth of these individual responses can account for the evolution of these surfaces.

[1] C. L. Kane and E. J. Mele, Quantum Spin Hall Effect in Graphene, Phys. Rev. Lett. **95**, 226801 (2005).

[2] C. L. Kane and E. J. Mele, Z_2 Topological Order and the Quantum Spin Hall Effect, Phys. Rev. Lett. **95**, 146802 (2005).

[3] B. A. Bernevig and S.-C. Zhang, Quantum Spin Hall Effect, Phys. Rev. Lett. **96**, 106802 (2006).

[4] B. A. Bernevig, T. L. Hughes, and S.-C. Zhang, Quantum spin hall effect and topological phase transition in HgTe quantum wells, Science **314**, 1757 (2006).

[5] L. Fu, C. L. Kane, and E. J. Mele, Topological Insulators in Three Dimensions, Phys. Rev. Lett. **98**, 106803 (2007).

[6] L. Fu, Topological Crystalline Insulators, Phys. Rev. Lett. **106**, 106802 (2011).

[7] T. H. Hsieh, H. Lin, J. Liu, W. Duan, A. Bansil, and L. Fu, Topological crystalline insulators in the SnTe material class, Nat. Commun. **3**, 982 (2012).

[8] Y. Tanaka, Z. Ren, T. Sato, K. Nakayama, S. Souma, T. Takahashi, K. Segawa, and Y. Ando, Experimental realization of a topological crystalline insulator in SnTe, Nat. Phys. **8**, 800 (2012).

[9] P. Dziawa, B. Kowalski, K. Dybko, R. Buczko, A. Szczerbakow, M. Szot, E. Łusakowska, T. Balasubramanian, B. M. Wojek, M. Berntsen, O. Tjernberg, and T. Story, Topological crystalline insulator states in $Pb_{1-x}Sn_xSe$, Nat. Mater. **11**, 1023 (2012).

[10] A. P. Schnyder, S. Ryu, A. Furusaki, and A. W. W. Ludwig, Classification of topological insulators and superconductors in three spatial dimensions, Phys. Rev. B **78**, 195125 (2008).

[11] A. Burkov, Topological semimetals, Nat. Mater. **15**, 1145 (2016).

[12] H. Gao, J. W. Venderbos, Y. Kim, and A. M. Rappe, Topological semimetals from first principles, Annu. Rev. Mater. Res. **49**, 153 (2019).

[13] A. Bernevig, H. Weng, Z. Fang, and X. Dai, Recent progress in the study of topological semimetals, J. Phys. Soc. Jpn. **87**, 041001 (2018).

[14] C. Fang, H. Weng, X. Dai, and Z. Fang, Topological nodal line semimetals, Chin. Phys. B **25**, 117106 (2016).

[15] J. Hu, S.-Y. Xu, N. Ni, and Z. Mao, Transport of topological semimetals, Annu. Rev. Mater. Res. **49**, 207 (2019).

[16] M. Z. Hasan and C. L. Kane, *Colloquium*: Topological insulators, Rev. Mod. Phys. **82**, 3045 (2010).

[17] Y. Ando and L. Fu, Topological crystalline insulators and topological superconductors: From concepts to materials, Annu. Rev. Condens. Matter Phys. **6**, 361 (2015).

[18] T. Ozawa, H. M. Price, A. Amo, N. Goldman, M. Hafezi, L. Lu, M. C. Rechtsman, D. Schuster, J. Simon, O. Zilberberg,

and I. Carusotto, Topological photonics, Rev. Mod. Phys. **91**, 015006 (2019).

[19] T. Ozawa and H. M. Price, Topological quantum matter in synthetic dimensions, Nat. Rev. Phys. **1**, 349 (2019).

[20] J. Dong, S. Zhou, T. Guan, H. Zhang, Y. Dai, X. Qiu, X. Wang, Y. He, X. Chen, and S. Li, Quantum Criticality and Nodal Superconductivity in the FeAs-Based Superconductor KFe_2As_2, Phys. Rev. Lett. **104**, 087005 (2010).

[21] G. M. Pang, M. Smidman, W. B. Jiang, J. K. Bao, Z. F. Weng, Y. F. Wang, L. Jiao, J. L. Zhang, G. H. Cao, and H. Q. Yuan, Evidence for nodal superconductivity in quasi-one-dimensional $K_2Cr_3As_3$, Phys. Rev. B **91**, 220502(R) (2015).

[22] C. Wang, H.-P. Sun, H.-Z. Lu, and X. Xie, 3D Quantum Hall Effect of Fermi Arcs in Topological Semimetals, Phys. Rev. Lett. **119**, 136806 (2017).

[23] R. A. Molina and J. González, Surface and 3D Quantum Hall Effects from Engineering of Exceptional Points in Nodal-Line Semimetals, Phys. Rev. Lett. **120**, 146601 (2018).

[24] Y. Zhang, Cyclotron orbit knot and tunable-field quantum Hall effect, Phys. Rev. Research **1**, 022005 (2019).

[25] C. Zhang, Y. Zhang, X. Yuan, S. Lu, J. Zhang, A. Narayan, Y. Liu, H. Zhang, Z. Ni, R. Liu, E. S. Choi, A. Suslov, S. Sanvito, L. Pi, H.-Z. Lu, A. C. Potter, and F. Xiu, Quantum Hall effect based on Weyl orbits in Cd_3As_2, Nature (London) **565**, 331 (2019).

[26] Y. S. Ang, C. H. Lee, and L. Ang, Universal scaling and signatures of nodal structures in electron tunneling from two-dimensional semimetals, arXiv:2003.14004.

[27] A. Bhattacharyya, P. Rodière, J.-B. Vaney, P. Biswas, A. Hillier, A. Bosin, F. Bernardini, S. Tencé, D. Adroja, and A. Cano, Evidence of nodal superconductivity in LaFeSiH, Phys. Rev. B **101**, 224502 (2020).

[28] T. Tuloup, R. W. Bomantara, C. H. Lee, and J. Gong, Nonlinearity induced topological physics in momentum space and real space, Phys. Rev. B **102**, 115411 (2020).

[29] L. Lu, L. Fu, J. D. Joannopoulos, and M. Soljačić, Weyl points and line nodes in gyroid photonic crystals, Nat. Photonics **7**, 294 (2013).

[30] M. Xiao, W.-J. Chen, W.-Y. He, and C. T. Chan, Synthetic gauge flux and Weyl points in acoustic systems, Nat. Phys. **11**, 920 (2015).

[31] Q. Lin, M. Xiao, L. Yuan, and S. Fan, Photonic Weyl point in a two-dimensional resonator lattice with a synthetic frequency dimension, Nat. Commun. **7**, 13731 (2016).

[32] Z. Yang and B. Zhang, Acoustic Type-II Weyl Nodes from Stacking Dimerized Chains, Phys. Rev. Lett. **117**, 224301 (2016).

[33] W.-J. Chen, M. Xiao, and C. T. Chan, Photonic crystals possessing multiple Weyl points and the experimental observation of robust surface states, Nat. Commun. **7**, 13038 (2016).

[34] M.-L. Chang, M. Xiao, W.-J. Chen, and C. T. Chan, Multiple Weyl points and the sign change of their topological charges in woodpile photonic crystals, Phys. Rev. B **95**, 125136 (2017).

[35] J. Noh, S. Huang, D. Leykam, Y. D. Chong, K. P. Chen, and M. C. Rechtsman, Experimental observation of optical Weyl points and Fermi arc-like surface states, Nat. Phys. **13**, 611 (2017).

[36] J. Y. Lin, N. C. Hu, Y. J. Chen, C. H. Lee, and X. Zhang, Line nodes, Dirac points, and Lifshitz transition in two-dimensional nonsymmorphic photonic crystals, Phys. Rev. B **96**, 075438 (2017).

[37] F. Li, X. Huang, J. Lu, J. Ma, and Z. Liu, Weyl points and Fermi arcs in a chiral phononic crystal, Nat. Phys. **14**, 30 (2018).

[38] B. Yang, Q. Guo, B. Tremain, R. Liu, L. E. Barr, Q. Yan, W. Gao, H. Liu, Y. Xiang, J. Chen, C. Fang, A. Hibbins, L. Lu, and S. Zhang, Ideal Weyl points and helicoid surface states in artificial photonic crystal structures, Science **359**, 1013 (2018).

[39] W. Gao, B. Yang, B. Tremain, H. Liu, Q. Guo, L. Xia, A. P. Hibbins, and S. Zhang, Experimental observation of photonic nodal line degeneracies in metacrystals, Nat. Commun. **9**, 950 (2018).

[40] X. Zhang, G. Li, Y. Liu, T. Tai, R. Thomale, and C. H. Lee, Tidal surface states as fingerprints of non-Hermitian nodal knot metals, Commun. Phys. **4**, 47 (2021).

[41] L. Xia, Q. Guo, B. Yang, J. Han, C.-X. Liu, W. Zhang, and S. Zhang, Observation of Hourglass Nodal Lines in Photonics, Phys. Rev. Lett. **122**, 103903 (2019).

[42] H. Zhou, J. Y. Lee, S. Liu, and B. Zhen, Exceptional surfaces in $\mathcal{PT}$-symmetric non-Hermitian photonic systems, Optica **6**, 190 (2019).

[43] C. H. Lee, A. Sutrisno, T. Hofmann, T. Helbig, Y. Liu, Y. S. Ang, L. K. Ang, X. Zhang, M. Greiter, and R. Thomale, Imaging nodal knots in momentum space through topolectrical circuits, Nat. Commun. **11**, 4385 (2020).

[44] A. Cerjan, S. Huang, M. Wang, K. P. Chen, Y. Chong, and M. C. Rechtsman, Experimental realization of a Weyl exceptional ring, Nat. Photonics **13**, 623 (2019).

[45] L. Li, C. H. Lee, and J. Gong, Emergence and full 3D-imaging of nodal boundary Seifert surfaces in 4D topological matter, Commun. Phys. **2**, 135 (2019).

[46] H. Jia, R. Zhang, W. Gao, Q. Guo, B. Yang, J. Hu, Y. Bi, Y. Xiang, C. Liu, and S. Zhang, Observation of chiral zero mode in inhomogeneous three-dimensional Weyl metamaterials, Science **363**, 148 (2019).

[47] G. Bian, T.-R. Chang, R. Sankar, S.-Y. Xu, H. Zheng, T. Neupert, C.-K. Chiu, S.-M. Huang, G. Chang, I. Belopolski, D. S. Sanchez, M. Neupane, N. Alidoust, C. Liu, B. Wang, C.-C. Lee, H.-T. Jeng, C. Zhang, Z. Yuan, S. Jia *et al.*, Topological nodal-line fermions in spin-orbit metal $PbTaSe_2$, Nat. Commun. **7**, 10556 (2016).

[48] T.-R. Chang, P.-J. Chen, G. Bian, S.-M. Huang, H. Zheng, T. Neupert, R. Sankar, S.-Y. Xu, I. Belopolski, G. Chang, B. Wang, F. Chou, A. Bansil, H.-T. Jeng, H. Lin, and M. Z. Hasan, Topological Dirac surface states and superconducting pairing correlations in $PbTaSe_2$, Phys. Rev. B **93**, 245130 (2016).

[49] A. Crepaldi, L. Moreschini, G. Autès, C. Tournier-Colletta, S. Moser, N. Virk, H. Berger, P. Bugnon, Y. J. Chang, K. Kern, A. Bostwick, E. Rotenberg, O. V. Yazyev, and M. Grioni, Giant Ambipolar Rashba Effect in the Semiconductor BiTeI, Phys. Rev. Lett. **109**, 096803 (2012).

[50] X. Zhang, L. Jin, X. Dai, and G. Liu, Topological type-II nodal line semimetal and Dirac semimetal state in stable kagome compound Mg_3Bi_2, J. Phys. Chem. Lett. **8**, 4814 (2017)PMID: 28927265.

[51] T.-R. Chang, I. Pletikosic, T. Kong, G. Bian, A. Huang, J. Denlinger, S. K. Kushwaha, B. Sinkovic, H.-T. Jeng, T. Valla, W. Xie, and R. J. Cava, Realization of a type-II nodal-

line semimetal in Mg_3Bi_2, Adv. Sci. (Weinheim) **6**, 1800897 (2019).

[52] T. Zhou, X.-G. Zhu, M. Tong, Y. Zhang, X.-B. Luo, X. Xie, W. Feng, Q. Chen, S. Tan, Z.-Y. Wang, T. Jiang, Y. Tang, X.-C. Lai, and X. Yang, Experimental evidence of topological surface states in Mg_3Bi_2 films grown by molecular beam epitaxy, Chin. Phys. Lett. **36**, 117303 (2019).

[53] J. Hu, Z. Tang, J. Liu, X. Liu, Y. Zhu, D. Graf, K. Myhro, S. Tran, C. N. Lau, J. Wei, and Z. Mao, Evidence of Topological Nodal-Line Fermions in ZrSiSe and ZrSiTe, Phys. Rev. Lett. **117**, 016602 (2016).

[54] L. Muechler, A. Topp, R. Queiroz, M. Krivenkov, A. Varykhalov, J. Cano, C. R. Ast, and L. M. Schoop, Modular Arithmetic with Nodal Lines: Drumhead Surface States in ZrSiTe, Phys. Rev. X **10**, 011026 (2020).

[55] L. M. Schoop, M. N. Ali, C. Straßer, A. Topp, A. Varykhalov, D. Marchenko, V. Duppel, S. S. Parkin, B. V. Lotsch, and C. R. Ast, Dirac cone protected by non-symmorphic symmetry and three-dimensional Dirac line node in ZrSiS, Nat. Commun. **7**, 11696 (2016).

[56] B.-B. Fu, C.-J. Yi, T.-T. Zhang, M. Caputo, J.-Z. Ma, X. Gao, B. Q. Lv, L.-Y. Kong, Y.-B. Huang, P. Richard, M. Shi, V. N. Strocov, C. Fang, H.-M. Weng, Y.-G. Shi, T. Qian, and H. Ding, Dirac nodal surfaces and nodal lines in ZrSiS, Sci. Adv., **5**, eaau6459 (2019).

[57] M. Novak, S. N. Zhang, F. Orbanić, N. Biliškov, G. Eguchi, S. Paschen, A. Kimura, X. X. Wang, T. Osada, K. Uchida, M. Sato, Q. S. Wu, O. V. Yazyev, and I. Kokanović, Highly anisotropic interlayer magnetoresitance in ZrSiS nodal-line Dirac semimetal, Phys. Rev. B **100**, 085137 (2019).

[58] S. Mardanya, B. Singh, S.-M. Huang, T.-R. Chang, C. Su, H. Lin, A. Agarwal, and A. Bansil, Prediction of threefold fermions in a nearly ideal Dirac semimetal BaAgAs, Phys. Rev. Mater. **3**, 071201(R) (2019).

[59] H. Weng, C. Fang, Z. Fang, and X. Dai, Topological semimetals with triply degenerate nodal points in θ-phase tantalum nitride, Phys. Rev. B **93**, 241202(R) (2016).

[60] Y.-H. Chan, C.-K. Chiu, M. Y. Chou, and A. P. Schnyder, Ca_3P_2 and other topological semimetals with line nodes and drumhead surface states, Phys. Rev. B **93**, 205132 (2016).

[61] L. S. Xie, L. M. Schoop, E. M. Seibel, Q. D. Gibson, W. Xie, and R. J. Cava, A new form of Ca_3P_2 with a ring of Dirac nodes, APL Mater. **3**, 083602 (2015).

[62] Y. K. Song, G. W. Wang, S. C. Li, W. L. Liu, X. L. Lu, Z. T. Liu, Z. J. Li, J. S. Wen, Z. P. Yin, Z. H. Liu, and D. W. Shen, Photoemission Spectroscopic Evidence for the Dirac Nodal Line in the Monoclinic Semimetal $SrAs_3$, Phys. Rev. Lett. **124**, 056402 (2020).

[63] S. Li, Z. Guo, D. Fu, X.-C. Pan, J. Wang, K. Ran, S. Bao, Z. Ma, Z. Cai, R. Wang, R. Yu, J. Sun, F. Song, and J. Wen, Evidence for a Dirac nodal-line semimetal in $SrAs_3$, Sci. Bull. **63**, 535 (2018).

[64] A. Yamakage, Y. Yamakawa, Y. Tanaka, and Y. Okamoto, Line-node Dirac semimetal and topological insulating phase in noncentrosymmetric pnictides CaAgX (X = P, As), J. Phys. Soc. Jpn. **85**, 013708 (2016).

[65] D. Takane, K. Nakayama, S. Souma, T. Wada, Y. Okamoto, K. Takenaka, Y. Yamakawa, A. Yamakage, T. Mitsuhashi, K. Horiba, H. Kumigashira, T. Takahashi, and T. Sato, Observation of Dirac-like energy band and ring-torus Fermi surface associated with the nodal line in topological insulator CaAgAs, npj Quantum Mater. **3**, 1 (2018).

[66] T. Nakamura, S. Souma, Z. Wang, K. Yamauchi, D. Takane, H. Oinuma, K. Nakayama, K. Horiba, H. Kumigashira, T. Oguchi, T. Takahashi, Y. Ando, and T. Sato, Evidence for bulk nodal loops and universality of Dirac-node arc surface states in ZrGeX_c (X_c = S, Se, te), Phys. Rev. B **99**, 245105 (2019).

[67] L. Guo, T.-W. Chen, C. Chen, L. Chen, Y. Zhang, G.-Y. Gao, J. Yang, X.-G. Li, W.-Y. Zhao, S. Dong, and R.-K. Zheng, Electronic transport evidence for topological nodal-line semimetals of ZrGeSe single crystals, ACS Appl. Electron. Mater. **1**, 869 (2019).

[68] S. Nie, Y. Sun, F. B. Prinz, Z. Wang, H. Weng, Z. Fang, and X. Dai, Magnetic Semimetals and Quantized Anomalous Hall Effect in EuB_6, Phys. Rev. Lett. **124**, 076403 (2020).

[69] R.-W. Zhang, Z. Zhang, C.-C. Liu, and Y. Yao, Nodal Line Spin-Gapless Semimetals and High-Quality Candidate Materials, Phys. Rev. Lett. **124**, 016402 (2020).

[70] D.-Y. Chen, Y. Wu, L. Jin, Y. Li, X. Wang, J. Duan, J. Han, X. Li, Y.-Z. Long, X. Zhang, D. Chen, and B. Teng, Superconducting properties in a candidate topological nodal line semimetal $SnTaS_2$ with a centrosymmetric crystal structure, Phys. Rev. B **100**, 064516 (2019).

[71] J. Gao, J. Si, X. Luo, J. Yan, Z. Jiang, W. Wang, C. Xu, X. Xu, P. Tong, W. Song, X. B. Zhu, W. J. Lu, and Y. P. Sun, Superconducting and topological properties in centrosymmetric $PbTaS_2$ single crystals, J. Phys. Chem. C **124**, 6349 (2020).

[72] B. Singh, S. Mardanya, C. Su, H. Lin, A. Agarwal, and A. Bansil, Spin-orbit coupling driven crossover from a starfruit-like nodal semimetal to Dirac and Weyl semimetal state in CaAuAs, Phys. Rev. B **98**, 085122 (2018).

[73] C.-J. Yi, B. Q. Lv, Q. S. Wu, B.-B. Fu, X. Gao, M. Yang, X.-L. Peng, M. Li, Y.-B. Huang, P. Richard, M. Shi, G. Li, O. V. Yazyev, Y.-G. Shi, T. Qian, and H. Ding, Observation of a nodal chain with Dirac surface states in Tib_2, Phys. Rev. B **97**, 201107(R) (2018).

[74] Z. Liu, R. Lou, P. Guo, Q. Wang, S. Sun, C. Li, S. Thirupathaiah, A. Fedorov, D. Shen, K. Liu, H. Lei, and S. Wang, Experimental Observation of Dirac Nodal Links in Centrosymmetric Semimetal TiB_2, Phys. Rev. X **8**, 031044 (2018).

[75] V. Jovic, R. J. Koch, S. K. Panda, H. Berger, P. Bugnon, A. Magrez, K. E. Smith, S. Biermann, C. Jozwiak, A. Bostwick, E. Rotenberg, and S. Moser, Dirac nodal lines and flat-band surface state in the functional oxide RuO_2, Phys. Rev. B **98**, 241101(R) (2018).

[76] X. Zhang, Z.-M. Yu, Z. Zhu, W. Wu, S.-S. Wang, X.-L. Sheng, and S. A. Yang, Nodal loop and nodal surface states in the Ti_3Al family of materials, Phys. Rev. B **97**, 235150 (2018).

[77] D. Shao, T. Chen, Q. Gu, Z. Guo, P. Lu, J. Sun, L. Sheng, and D. Xing, Nonsymmorphic symmetry protected node-line semimetal in the trigonal YH_3, Sci. Rep. **8**, 1467 (2018).

[78] Y. Xu, Y. Gu, T. Zhang, C. Fang, Z. Fang, X.-L. Sheng, and H. Weng, Topological nodal lines and hybrid Weyl nodes in $YCoC_2$, APL Mater. **7**, 101109 (2019).

[79] S.-S. Wang, Z.-M. Yu, Y. Liu, Y. Jiao, S. Guan, X.-L. Sheng, and S. A. Yang, Two-dimensional nodal-loop half-metal in monolayer MnN, Phys. Rev. Mater. **3**, 084201 (2019).

[80] G. Bian, T.-R. Chang, H. Zheng, S. Velury, S.-Y. Xu, T. Neupert, C.-K. Chiu, S.-M. Huang, D. S. Sanchez, I. Belopolski, N. Alidoust, P.-J. Chen, G. Chang, A. Bansil, H.-T. Jeng, H. Lin, and M. Z. Hasan, Drumhead surface states and topological nodal-line fermions in $TlTaSe_2$, Phys. Rev. B **93**, 121113(R) (2016).

[81] Q. Xu, R. Yu, Z. Fang, X. Dai, and H. Weng, Topological nodal line semimetals in the CaP_3 family of materials, Phys. Rev. B **95**, 045136 (2017).

[82] J. Ahn, D. Kim, Y. Kim, and B.-J. Yang, Band Topology and Linking Structure of Nodal Line Semimetals with Z_2 Monopole Charges, Phys. Rev. Lett. **121**, 106403 (2018).

[83] C. Niu, P. M. Buhl, G. Bihlmayer, D. Wortmann, Y. Dai, S. Blügel, and Y. Mokrousov, Two-dimensional topological nodal line semimetal in layered X_2Y ($X =$ Ca, Sr, and Ba; $Y =$ As, Sb, and Bi), Phys. Rev. B **95**, 235138 (2017).

[84] L. Li, C. H. Lee, and J. Gong, Realistic Floquet Semimetal with Exotic Topological Linkages between Arbitrarily Many Nodal Loops, Phys. Rev. Lett. **121**, 036401 (2018).

[85] M. R. Dennis, R. P. King, B. Jack, K. O'Holleran, and M. J. Padgett, Isolated optical vortex knots, Nat. Phys. **6**, 118 (2010).

[86] M. R. Dennis and B. Bode, Constructing a polynomial whose nodal set is the three-twist knot 52, J. Phys. A: Math. Theor. **50**, 265204 (2017).

[87] B. Bode and M. R. Dennis, Constructing a polynomial whose nodal set is any prescribed knot or link, J. Knot Theory Ramif. **28**, 1850082 (2019).

[88] G. Chang, S.-Y. Xu, X. Zhou, S.-M. Huang, B. Singh, B. Wang, I. Belopolski, J. Yin, S. Zhang, A. Bansil, H. Lin, and M. Z. Hasan, Topological Hopf and Chain Link Semimetal States and Their Application to Co_2MnGa, Phys. Rev. Lett. **119**, 156401 (2017).

[89] I. Belopolski, K. Manna, D. S. Sanchez, G. Chang, B. Ernst, J. Yin, S. S. Zhang, T. Cochran, N. Shumiya, H. Zheng, B. Singh, G. Bian, D. Multer, M. Litskevich, X. Zhou, S.-M. Huang, B. Wang, T.-R. Chang, S.-Y. Xu, A. Bansil *et al.*, Discovery of topological Weyl fermion lines and drumhead surface states in a room temperature magnet, Science **365**, 1278 (2019).

[90] Z. Li, Y. Xie, P.-Y. Chang, and Y. Chen, Interlocking nodal chains and their examples in carbon networks, Carbon **157**, 563 (2020).

[91] H. Yang and F. Wang, Conductivity in nodal line semimetals with short-ranged impurity potentials, arXiv:1908.01625.

[92] A. Laha, S. Malick, R. Singha, P. Mandal, P. Rambabu, V. Kanchana, and Z. Hossain, Magnetotransport properties of the correlated topological nodal-line semimetal YbCdGe, Phys. Rev. B **99**, 241102(R) (2019).

[93] E. Emmanouilidou, B. Shen, X. Deng, T.-R. Chang, A. Shi, G. Kotliar, S.-Y. Xu, and N. Ni, Magnetotransport properties of the single-crystalline nodal-line semimetal candidates $CaTX$ ($T =$ Ag, Cd; $X =$ As, Ge), Phys. Rev. B **95**, 245113 (2017).

[94] A. Laha, S. Mardanya, B. Singh, H. Lin, A. Bansil, A. Agarwal, and Z. Hossain, Magnetotransport properties of the topological nodal-line semimetal CaCdSn, Phys. Rev. B **102**, 035164 (2020).

[95] C. H. Lee, H. H. Yap, T. Tai, G. Xu, X. Zhang, and J. Gong, Enhanced higher harmonic generation from nodal topology, Phys. Rev. B **102**, 035138 (2020).

[96] D. Xiao, M.-C. Chang, and Q. Niu, Berry phase effects on electronic properties, Rev. Mod. Phys. **82**, 1959 (2010).

[97] H. M. Price, O. Zilberberg, T. Ozawa, I. Carusotto, and N. Goldman, Measurement of Chern numbers through center-of-mass responses, Phys. Rev. B **93**, 245113 (2016).

[98] I. Petrides, H. M. Price, and O. Zilberberg, Six-dimensional quantum Hall effect and three-dimensional topological pumps, Phys. Rev. B **98**, 125431 (2018).

[99] C. H. Lee, Y. Wang, Y. Chen, and X. Zhang, Electromagnetic response of quantum Hall systems in dimensions five and six and beyond, Phys. Rev. B **98**, 094434 (2018).

[100] M. Lohse, C. Schweizer, H. M. Price, O. Zilberberg, and I. Bloch, Exploring 4D quantum Hall physics with a 2D topological charge pump, Nature (London) **553**, 55 (2018).

[101] O. Schubert, M. Hohenleutner, F. Langer, B. Urbanek, C. Lange, U. Huttner, D. Golde, T. Meier, M. Kira, S. W. Koch, and R. Huber, Sub-cycle control of terahertz high-harmonic generation by dynamical Bloch oscillations, Nat. Photonics **8**, 119 (2014).

[102] H. Liu, Y. Li, Y. S. You, S. Ghimire, T. F. Heinz, and D. A. Reis, High-harmonic generation from an atomically thin semiconductor, Nat. Phys. **13**, 262 (2017).

[103] S. A. Mikhailov, Non-linear electromagnetic response of graphene, EPL **79**, 27002 (2007).

[104] Z. Cheng, Z. Zhang, H. Sun, S. Li, H. Yuan, Z. Wang, Y. Cao, Z. Shao, Q. Bian, X. Zhang, F. Li, J. Feng, S. Ding, Z. Mao, and M. Pan, Visualizing Dirac nodal-line band structure of topological semimetal ZrGeSe by ARPES, APL Mater. **7**, 051105 (2019).

[105] J. P. Lu, Elastic Properties of Carbon Nanotubes and Nanoropes, Phys. Rev. Lett. **79**, 1297 (1997).

[106] E. Pallecchi, A. C. Betz, J. Chaste, G. Fève, B. Huard, T. Kontos, J.-M. Berroir, and B. Plaçais, Transport scattering time probed through rf admittance of a graphene capacitor, Phys. Rev. B **83**, 125408 (2011).

[107] D. Y. H. Ho, I. Yudhistira, N. Chakraborty, and S. Adam, Theoretical determination of hydrodynamic window in monolayer and bilayer graphene from scattering rates, Phys. Rev. B **97**, 121404(R) (2018).

[108] G. Ndabashimiye, S. Ghimire, M. Wu, D. A. Browne, K. J. Schafer, M. B. Gaarde, and D. A. Reis, Solid-state harmonics beyond the atomic limit, Nature (London) **534**, 520 (2016).

[109] C. H. Lee, X. Zhang, and B. Guan, Negative differential resistance and characteristic nonlinear electromagnetic response of a topological insulator, Sci. Rep. **5**, 18008 (2015).

[110] M. Ezawa, Topological semimetals carrying arbitrary Hopf numbers: Fermi surface topologies of a Hopf link, Solomon's knot, trefoil knot, and other linked nodal varieties, Phys. Rev. B **96**, 041202(R) (2017).

[111] Y. Zhou, F. Xiong, X. Wan, and J. An, Hopf-link topological nodal-loop semimetals, Phys. Rev. B **97**, 155140 (2018).

[112] Z. Yan, R. Bi, and Z. Wang, Majorana Zero Modes Protected by a Hopf Invariant in Topologically Trivial Superconductors, Phys. Rev. Lett. **118**, 147003 (2017).

[113] An analogous approach [114] with complex singularities also does not allow for independent tuning of parameters.

[114] C. H. Lee, M. Claassen, and R. Thomale, Band structure engineering of ideal fractional Chern insulators, Phys. Rev. B **96**, 165150 (2017).